

Indirect measurements of the composition of ultrafine particles in the Arctic late-winter

Deanna Myers¹, Michael J. Lawler², Roy Mauldin³, Steven Sjostedt⁴, Manvendra K Dubey⁵, Jonathan P.D. Abbatt⁶, and James Smith²

¹Unknown

²University of California, Irvine

³University of Colorado Boulder

⁴Morgan Community College

⁵Los Alamos National Laboratory (DOE)

⁶University of Toronto

November 24, 2022

Abstract

We present indirect measurements of size-resolved ultrafine particle composition conducted during the Ocean–Atmosphere–Sea Ice–Snowpack (OASIS) Campaign in Utqiagvik, Alaska, during March 2009. This study focuses on measurements of size-resolved particle hygroscopicity and volatility measured over two periods of the campaign. During a period that represents background conditions in this location, particle hygroscopic growth factors (HGF) at 90% relative humidity ranged from 1.45–1.51, which combined with volatility measurements suggest a mixture of ~30% ammoniated sulfates and ~70% oxidized organics. Two separate regional ultrafine particle growth events were also observed during this campaign. Event 1 coincided with elevated levels of H₂SO₄ and solar radiation. These particles were highly hygroscopic (HGF=2.1 for 35 nm particles), but were almost fully volatilized at 160 °C. The air masses associated with both events originated over the Arctic Ocean. Event 1 was influenced by the upper marine boundary layer, while Event 2 spent more time closer to the surface and over open ocean leads, suggesting marine influence in growth processes. Event 2 particles were slightly less hygroscopic (HGF=1.94 for 35nm and 1.67 for 15nm particles), and similarly volatile. We hypothesize that particles formed during both events contained 60–70% hygroscopic salts by volume, with the balance for Event 1 being sulfates and oxidized organics for Event 2. These observations suggest that primary sea spray may be an important initiator of ultrafine particle formation events in the Arctic late-winter, but a variety of processes may be responsible for condensational growth.

1 **Indirect measurements of the composition of ultrafine particles in the Arctic late-winter**

2 **Deanna C. Myers¹, Michael J. Lawler¹, Roy L. Mauldin², Steven Sjostedt³, Manvendra Dubey⁴,**
3 **Jonathan Abbatt⁵, James N. Smith¹**

4 ¹Department of Chemistry, University of California, Irvine, CA, 92697, USA

5 ²Department of Atmospheric and Oceanic Sciences, University of Colorado, Boulder, CO, 80309, USA

6 ³Morgan Community College, Fort Morgan, CO, 80701, USA

7 ⁴Los Alamos National Laboratory, Los Alamos, NM, 87545, USA

8 ⁵Department of Chemistry, University of Toronto, Toronto, Ontario, M5S 3H6, Canada

9

10 **Abstract**

11 We present indirect measurements of size-resolved ultrafine particle composition conducted
12 during the Ocean–Atmosphere–Sea Ice–Snowpack (OASIS) Campaign in Utqiagvik, Alaska, during
13 March 2009. This study focuses on measurements of size-resolved particle hygroscopicity and volatility
14 measured over two periods of the campaign. During a period that represents background conditions in this
15 location, particle hygroscopic growth factors (HGF) at 90% relative humidity ranged from 1.45-1.51,
16 which combined with volatility measurements suggest a mixture of ~30% ammoniated sulfates and ~70%
17 oxidized organics. Two separate regional ultrafine particle growth events were also observed during this
18 campaign. Event 1 coincided with elevated levels of H₂SO₄ and solar radiation. These particles were
19 highly hygroscopic (HGF=2.1 for 35 nm particles), but were almost fully volatilized at 160 °C. The air
20 masses associated with both events originated over the Arctic Ocean. Event 1 was influenced by the upper
21 marine boundary layer, while Event 2 spent more time closer to the surface and over open ocean leads,
22 suggesting marine influence in growth processes. Event 2 particles were slightly less hygroscopic
23 (HGF=1.94 for 35nm and 1.67 for 15nm particles), and similarly volatile. We hypothesize that particles
24 formed during both events contained 60-70% hygroscopic salts by volume, with the balance for Event 1
25 being sulfates and oxidized organics for Event 2. These observations suggest that primary sea spray may
26 be an important initiator of ultrafine particle formation events in the Arctic late-winter, but a variety of
27 processes may be responsible for condensational growth.

28

29 **1 Introduction**

30 Aerosol particles in the Arctic are known to exhibit seasonal variability in their chemical and
31 physical properties. In many high-latitude regions, winter and early spring are dominated by Arctic Haze,
32 a phenomenon characterized by long-range transport of anthropogenic pollutants and resulting in the
33 highest mass concentrations of particulate matter (Barrie, 1986; Rahn, 1981; Tunved et al., 2013).
34 Accumulation mode particles dominate during this period, largely from transport of anthropogenic
35 pollution originating from Eurasia (Barrie, 1986; Frossard et al., 2011; Heintzenberg, 1982; Law & Stohl,
36 2007; Quinn et al., 2017; Rahn, 1981; Tunved et al., 2013). A persistent boundary layer effectively traps
37 pollution over the Arctic, coastal Eurasia, and much of Canada until late spring, when it recedes to polar
38 north (Barrie, 1986). Late spring and summer are less anthropogenically-influenced, and thus are
39 characterized by lower particle concentrations (Browse et al., 2012; Croft et al., 2016; Garrett et al., 2011;
40 Ström et al., 2003; Tunved et al., 2013). During that period, marine biogenic emissions and
41 photochemistry are key drivers of atmospheric chemistry (Dall'Osto, et al., 2018; Quinn et al., 2002;
42 Tunved et al., 2013).

43 Several recent studies have shown that the formation and growth of sub-100 nm diameter
44 ultrafine particles (UFP) occur readily in the Arctic atmosphere (Allan et al., 2015; Asmi et al., 2016;
45 Baccarini et al., 2020; Chang et al., 2011; Collins et al., 2017; Dall'Osto et al., 2017; Dall'Osto et al.,
46 2018; Giamarelou et al., 2016; Heintzenberg et al., 2015; Karl et al., 2013, 2012; Kecorius et al., 2019;
47 Kolesar et al., 2017; Kupiszewski et al., 2013; Nguyen et al., 2016; Tunved et al., 2013; Willis et al.,
48 2016; Ziemba et al., 2010). However, few to date have focused on the composition of Arctic UFP and
49 most observations have occurred during summer. Prior spring and summer studies have attributed UFP
50 formation events to photochemical sulfuric acid (H_2SO_4) production (Covert & Heintzenberg, 1993), with
51 sulfate considered an important particle component (Nyeki et al., 2005; Wiedensohler et al., 1996). These
52 employed filters and impactors for offline chemical analysis, biasing these results to larger particles that
53 may not represent the composition of UFPs. Size-resolved nanoparticle composition of Arctic UFPs has
54 been studied using mostly indirect measurements, with a focus on formation and growth events during
55 late spring and summer. In the Canadian Arctic, UFP formation was observed to occur freely in the
56 marine boundary layer, with complementary gas-phase measurements suggesting marine biogenic sources
57 of organic and sulfur-containing gas-phase precursors (Burkart et al., 2017). Several observations of UFP
58 formation and growth from other Arctic locations associated these phenomena with oxidized products of
59 dimethylsulfide (DMS) like methanesulfonic acid (MSA) and H_2SO_4 , suggesting a marine biogenic
60 influence (Abbatt et al., 2019; Chang et al., 2011; Dall'Osto et al., 2018; Ferek et al., 1995;
61 Ghahremaninezhad et al., 2016; Leaitch et al., 2013; Quinn et al., 2002). Indirect measurements of

62 summertime particle composition in Ny-Alesund, Svalbard, indicated that organic vapor condensation
63 plays a large role in UFP formation (Kecorius et al., 2019). Organic compounds were found to contribute
64 to the growth of newly formed UFPs in the Canadian Arctic, with a small contribution from sulfur-
65 containing compounds (Tremblay et al., 2019). Willis et al., (2016) showed that growth of sub-20 nm
66 particles to ~50 nm coincided with the presence of organics, trimethylamine, and MSA in particles 80 nm
67 and larger, suggesting the particles grew by condensation of MSA and other lower-volatility organic
68 species. Model results from Canadian Arctic observations using a paired chemical transport-microphysics
69 model indicate that ternary nucleation from H₂SO₄, ammonia (NH₃), and water, followed by condensation
70 from marine biogenic species and biogenically derived sulfur compounds, accounts for more than 90% of
71 the simulated number concentration for particles larger than 20 nm (Croft et al., 2019). Other
72 measurements performed in late-summer suggest that iodine (Allan et al., 2015; Baccarini et al., 2020)
73 and marine nanogels are responsible for some observed UFP formation events (Dall'Osto et al., 2017;
74 Karl et al., 2013; C Leck et al., 2013; Caroline Leck & Bigg, 2010). Measurements made during 11
75 particle formation events aboard the Swedish icebreaker *Oden* in August and September of 2018 found
76 that these events coincided with elevated levels of iodic acid (HIO₃) and relatively low levels of H₂SO₄
77 (Baccarini et al., 2020). Fragmentation of primary marine biological particles, where nano-granules are
78 released from evaporation of cloud/fog droplets while H₂SO₄ nucleates to form clusters, both grow
79 through condensation of low-volatility vapors, and then coagulate to form particles larger than 3nm, has
80 been proposed to explain numerous UFP formation events observed in the high Arctic during late spring
81 and summer (Karl et al., 2013). Taken together, these results suggest gas-phase ammonia, amines,
82 organics, oxidized sulfur species, and fragmentation of primary marine particles contribute to the
83 formation and growth of UFPs in the late spring and early summer in this region.

84 Winter and early spring measurements of UFP formation events and the composition of these
85 particles are largely missing. This is due in part to the dominant accumulation mode that biases bulk and
86 sub-micron measurements towards larger particles. Some insights into the mechanisms of UFP formation
87 can nonetheless be gained through such measurements. Analysis of sub-micron aerosol particle
88 composition during particle formation events in Tiksi, Siberia, made by aerosol mass spectrometry
89 (AMS) found that while summertime events were driven by oxidation of biogenic low-volatility gases,
90 early spring events are likely due to oxidation of anthropogenic precursors of Arctic Haze (Asmi et al.,
91 2016). Filter samples have shown submicron particles are largely composed of sea salt and non-sea-salt
92 sulfates (nss sulfate) (Kirpes et al., 2018, 2019; Patterson et al., 1967; Quinn et al., 2002; Tomasi et al.,
93 2012). Long-term measurements taken at Utqiagvik (formerly Barrow), Alaska are consistent with other
94 measurements indicating nss sulfate is a major component of submicron wintertime aerosol, but the
95 concentration decreased by ~60% between 1976 and 2008. Elemental analysis indicated that while source

96 regions remained the same over this time period, emissions decreased (Quinn et al., 2009). Soot particle
97 AMS (SP-AMS) measurements made in Greenland have linked UFP formation in February through May
98 to MSA and molecular iodine, suggesting contributions from both biotic and abiotic sources (Dall'Osto,
99 et al., 2018). Since most winter-time measurements to date have been performed on bulk aerosol, Arctic
100 UFP composition is still not understood in the winter and early spring. More measurements are needed in
101 order to understand the mechanisms by which new particles form in this important region.

102 We seek to address this measurement gap by reporting indirect measurements of UFP
103 composition made during the Ocean – Atmosphere – Sea Ice – Snowpack (OASIS) Campaign in
104 Utqiagvik, Alaska during March 2009. A period from 27 – 31 March was determined to have winds from
105 the Arctic Ocean, with particle properties measured during this time representing background conditions.
106 Two separate nanoparticle growth events were observed during this that campaign (12 -14 March), where
107 particles grew from 5 nm to ~ 20 nm in diameter. Size-resolved hygroscopicity and volatility measured
108 during these events were analyzed to hypothesize the species involved the growth of these newly formed
109 particles.

110 **2 Methods**

111 **2.1 Site description**

112 Measurements were made during the OASIS field campaign in Utqiagvik, Alaska during March
113 and April 2009. The focus of this paper is on two periods – one that featured measurements of two
114 separate UFP growth events occurring during 12 – 14 March, and a second background period from 27 –
115 31 March. All times are reported in Alaska Daylight Time (AKDT; UTC – 8 hours) and are referred to as
116 “local time” in this work. Particle measurements were collected in a Quonset hut at the U.S. Navel Arctic
117 Research Laboratory (NARL) and trace gas and surface meteorology measurements were performed
118 approx. 1 km away in buildings located near the Barrow Arctic Research Center (BARC). Numerous
119 measurements of key trace gases and particle properties, as well as of meteorology, were made over the
120 course of the campaign; those pertinent during the time periods of interest are outlined below.

121 **2.2 Air mass origin and station meteorology**

122 Air mass backward trajectories were calculated to determine source influences for each of the
123 ultrafine particle events observed using the NOAA Hybrid Single-Particle Lagrangian Integrated
124 Trajectory (HYSPLIT) transport model (Rolph et al., 2017; Stein et al., 2015). Backward trajectories of
125 72-hour duration were determined for air masses arriving 50 meters above ground level (AGL) at the
126 measurement site at the beginning and halfway through the UFP events (Event 1: 3/12/09 04:07 – 19:02

127 ADT; Event 2: 3/13/09 20:37 – 3/14/09 3:47 ADT) using the Global Data Assimilation System (GDAS)
128 1° meteorology. Satellite images from NASA Moderate Resolution Imaging Spectroradiometer
129 (MODIS)/Aqua Sea Ice Extent with temporal resolution of 5 minutes and spatial resolution of 1 kilometer
130 were used to identify leads and areas of open water in the sea ice (Hall & Riggs, 2015). Images were
131 analyzed for 10 – 14 March, corresponding to the timespan of the HYSPLIT back trajectories calculated
132 for each UFP growth event observed.

133 Sonic anemometers (Applied Technologies, Sonic Anemometer/Thermometer model SATI/3K)
134 were used to measure three-dimensional wind velocities at 10 Hz. Wind speed and direction were
135 obtained from vector-averaging the horizontal wind velocities over 1-minute intervals and are accurate to
136 $\pm 0.03 \text{ m s}^{-1}$ and $\pm 0.1^\circ$, respectively. Wind direction data are color-coded to identify periods with likely
137 local influences at the measurement sites (labelled “Utqiagvik”, “local building” and “local NNW”) and
138 periods with minimal local influence (labelled “clean”). Time periods with “calm” winds were those with
139 minimal wind.

140 Solar radiation was measured at the NOAA Barrow Atmospheric Baseline Observatory,
141 approximately 3.5 km northeast of NARL. We report 1-minute measurements of downwelling global
142 solar radiation (W m^{-2}), performed with an unshaded Precision Spectral Pyranometer (Eppley).

143 **2.3 Particle physical, chemical, and radiative properties**

144 2.3.1 Particle number size distributions

145 Particle number size distributions for particles with electrical mobility diameter of 4 nm to 1 μm
146 were collected using a particle size distribution system consisting of 3 instruments that measure with a 5-
147 minute time resolution. A nanometer scanning mobility particle sizer (nano-SMPS) comprised of a home-
148 built bipolar neutralizer, a TSI model 3085 Differential Mobility Analyzer (DMA), a home-built high
149 voltage and flow control system, and an Ultrafine Condensation Particle Counter (UCPC, TSI model
150 3025a), covered the particle mobility range of 4 to 30 nm. A scanning mobility particle sizer (SMPS),
151 identical to the nano-SMPS except for the use of a TSI model 3081 DMA and a standard condensation
152 particle counter (CPC, TSI model 7620, modified to run at 1.2 lpm aerosol flow rate), measured particles
153 of diameter ~ 22 to ~ 225 nm. An optical particle counter (OPC, Lasair model 1002 PMS, Inc.) measured
154 particle number-size distributions over the diameter range of 0.1 to 1 μm . Measured distributions were
155 combined to create a continuous size distribution, which was used also in calculations of particle growth
156 rates following the method outlined in Dal Maso et al. (2005) and gamma (Γ ; Section 3.3) (Kuang et al.,
157 2010). Size distributions were corrected for the transmission efficiency of the inlet tubing using

158 theoretically predictions that assume laminar flow, the latter of which was confirmed by our inlet flow
159 rate measurements (Hinds, 1999).

160 2.3.2 Particle optical properties

161 Bulk ambient particle absorption and scattering coefficients were measured at 781 nm using a
162 photoacoustic soot spectrometer (PASS-1, Droplet Measurement Technologies using principles and
163 protocols described in Flowers et al. (2010). Aerosol particle absorption coefficients (β_{abs}) at 781 nm were
164 directly measured using the photoacoustic technique and scattering coefficients (β_{sca}) were measured
165 simultaneously on the same dry aerosol sample with an integrating nephelometer. Noise was removed
166 from collected data using a bandpass filter, with a band set between 0 and 12 $M\ m^{-1}$ for scattering data,
167 and 0 and 30 $M\ m^{-1}$ for the absorption data. The instrument was zeroed every 40 minutes to eliminate
168 systematic drifts and the reported measurements were averaged in 150 second bins to enhance signal to
169 noise. Particle single scattering albedo (SSA) was calculated as follows:

$$170 \quad SSA = \frac{\beta_{sca}}{\beta_{sca} + \beta_{abs}} \quad (1)$$

171 Calculated values of SSA were used to determine the relative absorbing versus scattering properties of
172 bulk particles during periods of interest and were also used to identify periods of local pollution such as
173 that provided by snow removal equipment that have low SSA due to absorbing soot emissions, which
174 would not have been identified from wind direction measurements.

175 2.3.3 Indirect measurements of particle chemical properties

176 A hygroscopicity tandem differential mobility analyzer (HTDMA) measured the hygroscopic
177 growth factor of size-selected particles at 90% relative humidity (RH). In this home-built instrument,
178 which is also described in detail elsewhere (Lance et al., 2013), particles were neutralized with a unipolar
179 neutralizer, dried to ~2% RH, and then size-selected by the first DMA (home-built, but identical in design
180 to TSI model 3081). Dry particle sizes studied had electrical mobility diameters ($Dp(RH_{dry})$) of 15, 35, 50,
181 75, and 110 nm. Size-selected particles then passed to the conditioning chamber, where they were
182 exposed to a controlled 90% RH. The resulting size distribution was measured by a second, identical
183 DMA and a CPC (TSI model 3010). Sheath and excess flows in the DMAs were 5 lpm with an aerosol
184 flow of 0.6 lpm. Data was corrected for variations in relative humidity in the second DMA using methods
185 outlined in Gysel et al. (2009) and Keith and Arons (1954). All corrected size distributions during the
186 periods discussed below consisted of a single mode, suggesting internally mixed aerosol. These size
187 distributions were fitted with a Gaussian curve and the peak of the curve was used to represent the peak
188 diameter of the humidified mode $Dp(RH_{humid})$. Hygroscopic growth factor (HGF) was calculated using:

189
$$HGF = \frac{Dp(RH_{humid})}{Dp(RH_{dry})} \quad (2)$$

190 From measurements of HGF , we then estimate the volume fraction of representative particulate
 191 compounds using the Zdanovskii-Stokes-Robinson (ZSR) relation:

192
$$HGF_{meas} = (\sum_k \varepsilon_k HGF_k^3)^{1/3}$$

193 where ε_k is the volume fraction of pure component k in the particle and HGF_k is the growth factor of pure
 194 component k (Malm & Kreidenweis, 1997; Stokes & Robinson, 1966).

195 A volatility TDMA (VTDMA) measured the volatility of size-selected particles at different
 196 temperatures. Ambient particles were neutralized and size-selected by the first DMA (TSI model 3081) at
 197 mobility diameters of 15, 35, 75, 110, and 165 nm. Particles then passed through a fast stepping/scanning
 198 thermodenuder built by Aerodyne Research, Inc., and modeled after the system described by Huffman et
 199 al. (2008). The thermodenuder was stepped at temperatures of $T_D = 30, 40, 80, \text{ and } 160 \text{ }^\circ\text{C}$, and time was
 200 allowed during each step for the temperature to stabilize before measurement. The particle number size
 201 distribution was measured with the second DMA (TSI model 3081) and CPC (TSI model 3010). The
 202 sample flow rate through the denuder was set to 0.6 LPM, which was determined to be optimal for this
 203 design by Wehner et al. (2002). Like the HTDMA, sheath flows in the DMAs were 5 lpm with a particle
 204 flow of 0.6 lpm. Data are reported at each temperature as the volume fraction remaining, VFR , which is
 205 defined as:

206
$$VFR = \frac{V_T}{V_{30^\circ\text{C}}} \quad (3)$$

207 where V_T is the integrated total particulate volume (assuming spherical particles) at temperature, T . We
 208 note that ambient atmospheric temperatures during the measurement periods generally ranged from -20 to
 209 -30 $^\circ\text{C}$ while the VTDMA maintained a temperature within the Quonset hut of $\sim 14 \text{ }^\circ\text{C}$, likely leading to
 210 evaporation of some particulate compounds prior to the initial size-selection. For this reason, and because
 211 the Quonset hut temperature was poorly controlled, we chose to divide V_T by the integrated volume of
 212 particles exposed to our lowest controlled temperature, 30 $^\circ\text{C}$ ($V_{30^\circ\text{C}}$), in our calculations of VFR. Prior to
 213 analysis, some instrument noise was easily identified in data as repetitive modes present throughout the
 214 sampling and calibration periods and was consequently removed.

215 Both the HTDMA and VTDMA were calibrated at the site, before and after the observation
 216 period, using ammonium sulfate aerosol that was aerosolized using a commercial aerosol generator (TSI
 217 model 3076). These experiments confirmed that both instruments were operating properly and that no
 218 further adjustments to the data, other than those described above, were needed.

219 **2.4 Trace Gas Analysis**

220 Gas-phase concentration measurements of H₂SO₄, OH, and MSA were obtained using a selected
221 ion chemical ionization mass spectrometer (SICIMS). Measurements were made using an inlet ~ 1.5 m
222 above the snow surface in a building located ~ 500 m east of the particle measurement location. Details of
223 this instrument have been previously reported in Tanner et al., (1997) and Mauldin et al., (1998). Data
224 were calibrated and are presented as 30-second averages.

225 **3 Results and Discussion**

226 **3.1 Campaign overview**

227 The OASIS Campaign took place from late February through mid-April 2009, with particle
228 measurements beginning on 5 March. The foci of the campaign were on gas-phase exchanges between the
229 ocean, atmosphere, sea ice, and snowpack, the impact of these processes on oxidation capacity in the
230 remote Arctic atmosphere, and how they may change with a changing climate (NCAR, 2012). The
231 measurement period during late winter and early spring is chemically interesting because of the
232 appearance of light at the end of polar winter (Barrie, 1986). With increasing solar radiation during the

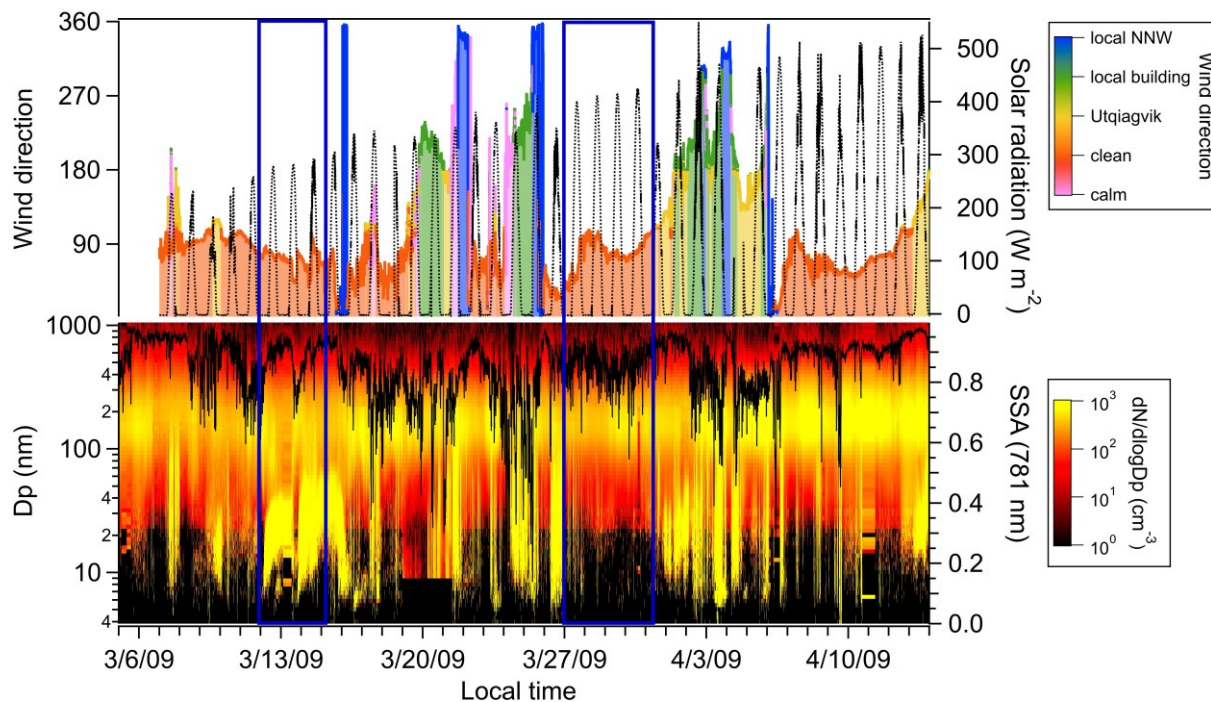


Figure 1. Meteorological data and bulk particle properties during the entire OASIS observation period. Plotted above are wind direction (color-coded to show relative direction of origin) and downwelling solar radiation. The lower plot is the particle number size distribution (diameters 4 to 1000 nm) and single scattering albedo (SSA) measured at 781 nm (black). The focus of this work is a background period (27 – 31 March) and two distinct ultrafine particle growth events (12 – 14 March), which are boxed in blue.

233 course of this campaign, photochemistry became progressively more important during the observation
234 period (Fig. 1). Several major findings from OASIS have thus far related to gas-phase photochemical
235 halogen chemistry, with a particular focus on bromine, including its efficacy in ozone (O_3) depletion
236 compared to chlorine (Thompson et al., 2015) and its recycling process (Frieß et al., 2011; Liao et al.,
237 2012).

238
239 Throughout the course of the campaign, there are two prominent features in the particle size
240 distribution measurements: sub-20 nm particles appear at the site at an initial diameter of 5 nm in bursts,
241 with no *in situ* nucleation observed at the site as evidenced by the lack of sub-5 nm diameter particles;
242 and a continuous mode centered at 200 nm (Figure 1). Note that the campaign-averaged value of SSA is
243 ~ 0.8 , with decreases to values ~ 0.5 during periods with “local building” and “local NNW” influence
244 (Figure 1). This indicates that local particle emissions are more highly absorbing than ambient Arctic
245 particles in this region, which has been observed in numerous Arctic sites during this time of year
246 (Bodhaine et al., 1981; Clarke et al., 1984; Patterson et al., 1967; Polissar et al., 2001; Tomasi et al.,
247 2012).

248

249 **3.2 Background period**

250 We begin by reporting measurements made during a period (27 – 31 March) that we identified as
251 “clean” in order to explore regional Arctic UFP physico-chemical properties and address the lack of
252 winter and spring observations. Figure 2 shows a summary of the data that include, to the best of our
253 knowledge, the first indirect composition measurements of size-selected, sub-500 nm atmospheric
254 particles in the Utqiagvik area. Bulk SSA was, on average, 0.861 ± 0.055 , indicating internally mixed
255 black carbon (BC) in this region, and showed relatively low variability, suggesting that local emissions
256 did not substantially bias our measurements during this period. Like the rest of the campaign, sub-20 nm
257 particle concentrations were very low with total number concentration during the period averaging 380
258 cm^{-3} . In comparison to other Arctic measurements made in March, this is lower than the concentration
259 measured in Siberia (Asmi et al., 2016), but about twice as high as that observed in Svalbard (Tunved et
260 al., 2013) and Greenland (Nguyen et al., 2016). These differences in particle concentration exemplify the
261 variability in particle properties throughout different Arctic locations.

262 Figure 2c shows *HGF* measured at 90% RH for 35, 75, and 110 nm size-selected ambient
263 particles. Data for 15 nm particles are missing for both HTDMA and VTDMA instruments due to the
264 extremely low concentrations of these particles. The figure also includes published *HGF* data for
265 laboratory-generated sea salt aerosol ($D_p = 50$ nm) (Zieger et al., 2017), ammonium sulfate (Asmi et al.,
266 2010; Hämeri et al., 2000; Sjogren et al., 2007), black carbon (Weingartner et al., 1995), and a seawater

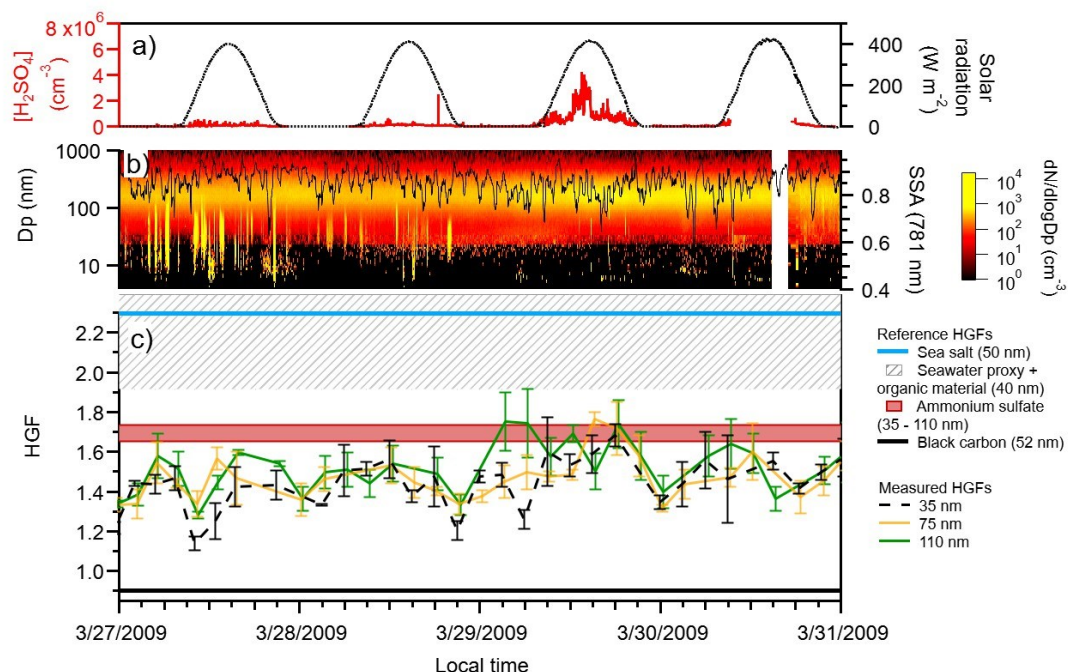


Figure 2. Particle properties measured during the background period, showing (a) H_2SO_4 concentration (red), downwelling solar radiation (black); (b) particle size distribution for particle sizes between 4 and 1000 nm in diameter, and single scattering albedo (black); and (c) measured particle growth factors for 35 nm (black, dashed), 75 nm (gold), and 110 nm (green, dashed) particles. Also plotted are reference growth factors for sea salt (light blue; Zieger et al., 2017), seawater proxy with organic material (gray hashed; Fuentes et al., 2011), ammonium sulfate (red, 35 – 110 nm size selected; Hämeri et al., 2000), and black carbon (black, Weingartner et al., 1995).

267 proxy containing varying amounts of organic material ($D_p = 40$ nm) (Fuentes et al., 2011). For the
 268 duration of the background period, ambient particles were less hygroscopic than sea salt and seawater
 269 proxy references, with average HGF s of 1.45 ± 0.12 ($D_p = 35$ nm), 1.48 ± 0.11 ($D_p = 75$ nm), and $1.51 \pm$
 270 0.12 ($D_p = 110$ nm) measured. There is a small degree of size-dependence on HGF during this period,
 271 although the values and their respective standard deviations all lie within the same range.

272 Figure 3 shows the VFR for ambient 35, 75 and 110 nm size-selected particles. Negligible particle
 273 volume is lost at all sizes upon heating to 40 °C (3.52 ± 0.011 %, 3.53 ± 0.20 % and 2.54 ± 0.78 %, respectively),
 274 which corresponds to the loss of higher-volatility compounds such as semivolatile organics
 275 (Burtscher et al., 2001; Häkkinen et al., 2012; Kreidenweis et al., 1998). Volume loss at 80 °C, indicative
 276 of evaporation of lower-volatility organic species (Burtscher et al., 2001; Häkkinen et al., 2012;
 277 Kreidenweis et al., 1998) and certain higher volatility inorganic salts (Bergin et al., 1997), accounts for
 278 80.8 ± 0.2 % of the volume for sampled 35 nm particles, 84.3 ± 0.2 % of the volume for sampled 75 nm
 279 particles and 65.7 ± 0.9 % of the volume for 110 nm sampled particles. Nearly all particle volume was
 280 lost upon heating to 160 °C; at this temperature, 3.0 ± 0.1 % of the total volume of 35 nm size-selected
 281 particles, 2.9 ± 0.2 % of the total volume of 75 nm size-selected particles and 4.7 ± 2.3 % of the total

282 volume of 110 nm size-selected particles remained. This likely is BC and may explain the average SSA
283 values measured during this time period, which indicate that BC is internally mixed in bulk aerosol.
284

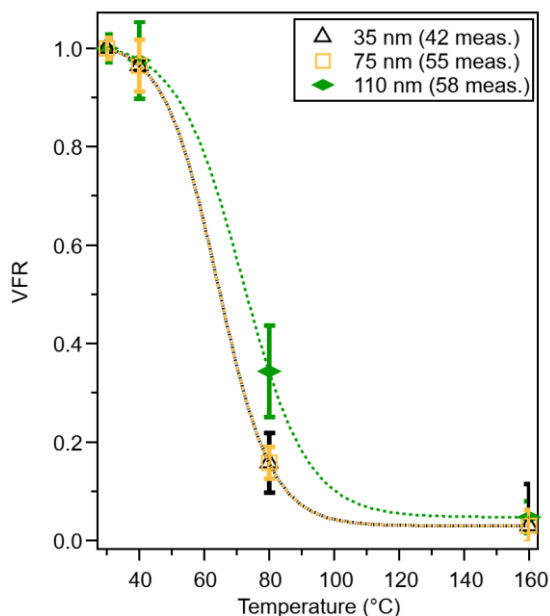


Figure 3. Average volume fraction remaining at 40, 80, and 160 °C for 35, 75 and 110 nm size-selected particles during the background period (27 – 31 March) with sigmoidal fits to data. The error bars represent standard deviation and the number of measurements at each size is shown in the legend. Initial volume ($VFR = 1$) is assumed to be the volume at 30 °C.

Combining the results of the *HGF* and *VFR* analyses provides insights into the composition of background UFPs. The high volume loss of particles at 80 °C makes it unlikely that a significant fraction of UFP volume consists of low-volatility inorganic salts. This is supported by the *HGF* analysis that shows significantly lower hygroscopicity compared to sea salt and seawater proxy reference particles (Figure 2c). The observed evaporation behavior is consistent with sulfate that is partially or fully neutralized by a base such as ammonia, which is expected to fully evaporate at temperatures below 160 °C as confirmed by our calibrations as well as those performed by Huffman et al., (2008) using a similar instrument. The measured *HGF* is slightly below than that of ammonium sulfate (Figure 2c) with the exception of a period of elevated gas phase H_2SO_4 on 29 March during which *HGF* increased slightly, supporting a contribution of sulfate to UFP

304 composition with the addition of a less hygroscopic material. This leads us to hypothesize that UFPs also
305 contain some fraction of lower hygroscopicity organics. Organic compounds are routinely detected in
306 marine aerosol (Cochran et al., 2017; O’Dowd et al., 2004; Prather et al., 2013). A mixture of organics
307 and sulfate is also consistent with the measured *VFR* data, as loss of particulate volume over the size
308 range of 40 – 160 °C is consistent not only with ammonium sulfate but with oxidized organics (Huffman
309 et al., 2009). Our measurements suggest that, while it may be possible that primary organics contribute to
310 background UFP composition, the observation that *VFR* is nearly zero at 160 °C suggests minimal
311 contribution from low-volatility primary marine organic species (Frossard et al., 2014), and a small
312 contribution from black carbon (Jennings et al., 1994). The measured *HGFs* may be consistent with that
313 measured for marine nanogels (Hawkins & Russell, 2010; Ovadnevaite et al., 2011), the latter of which
314 ranged from 1.2 to 1.3 at 90% RH.

315 An estimate of the volume fractions of sulfate salt and organic species, using the *HGFs* of
316 ammonium sulfate (1.7) (Hämeri et al., 2000) and atmospheric organic matter (1.2) (Gysel et al., 2004),
317 was performed using the average ambient *HGF* measured for each particle size reported above. Using the
318 ZSR method with these assumptions, we estimate that, on average, volume fractions of ammonium sulfate
319 (ϵ_{AS}) and organic species (ϵ_{ORG}) were 0.48 and 0.52 for 35 nm particles, 0.44 and 0.56 for 75 nm particles,
320 and 0.50 and 0.50 for 110 nm particles, respectively. Estimations of volume fraction using H_2SO_4 as a
321 third component ($HGF = 1.9$, ϵ_{SA}) were more consistent with the *VFR* measured for the larger particle
322 sizes; for 35 nm, $\epsilon_{AS} = 0.10$, $\epsilon_{SA} = 0.20$, $\epsilon_{ORG} = 0.70$; for 75 nm, $\epsilon_{AS} = 0.10$, $\epsilon_{SA} = 0.23$, $\epsilon_{ORG} = 0.67$; and
323 for 110 nm, $\epsilon_{AS} = 0.10$, $\epsilon_{SA} = 0.27$, $\epsilon_{ORG} = 0.63$. These estimates support the hypothesis that partially
324 neutralized sulfate and organic species contribute mainly to the observed UFP volume.

325

326 3.3 Ultrafine particle growth events

327 In mid-March there were two distinct UFP growth events observed at the site occurring on
328 consecutive days (Figure 4). Both occurred during a “clean” period and there was no evidence in SSA
329 data (Event 1: 0.845 ± 0.076 ; Event 2: 0.857 ± 0.030) to suggest any site-specific pollution impacting the
330 particle properties measured. Bulk particle SSA measured during both periods were very similar to both
331 each other and the background period average. Event 1 was first observed at the site at just after 4:00
332 local time on 12 March, with particles appearing at a modal diameter of 11 nm. The modal diameter
333 increased linearly over a 12-hour period to 21 nm, corresponding to a growth rate 0.862 ± 0.034 nm h⁻¹.
334 This event coincided with solar radiation at the site and an average measured H_2SO_4 concentration of
335 3.7×10^6 molecules cm⁻³. Event 2 was first observed at the site on 13 March at 20:40, with a measured
336 modal diameter of 7 nm. Growth lasted for ~4 hours ending at 15 nm and a measured modal growth rate
337 of 2.12 ± 0.07 nm h⁻¹. This mode persisted after midnight, but no longer displayed growth. The event
338 occurred at nighttime, thus solar radiation was minimal and the average concentration of H_2SO_4 was
339 3.0×10^5 molecules cm⁻³, which is close to the SICIMS lower limit of detection.

340 A prior analysis of ultrafine particle growth rates observed at the NOAA Research Station at
341 Utqiagvik characterized these two growth events as “marine influenced” along with possible influence
342 from Prudhoe Bay (Kolesar et al., 2017). To provide additional insights into the origins of these air
343 masses, 72-hour HYSPLIT back trajectories were calculated for the period of each event before their
344 arrival at the measurement site and are overlaid over MODIS satellite images of the region in Figure 5.
345 There were no significant changes in the sea ice in this region over the time periods of the back
346 trajectories, so the satellite image shown, while from 11 March, is representative of the entire modeling
347 period (10 – 14 March). Two traces are shown for each event, with the starting point of the back
348 trajectory corresponding to the beginning and halfway time points of the events. The black boxes on

349 Figure 5 indicate areas of direct ocean-atmosphere interfaces in the sea ice, both in the form of open
 350 leads, which are small regions of water between ice sheets that serve as direct interfaces between the

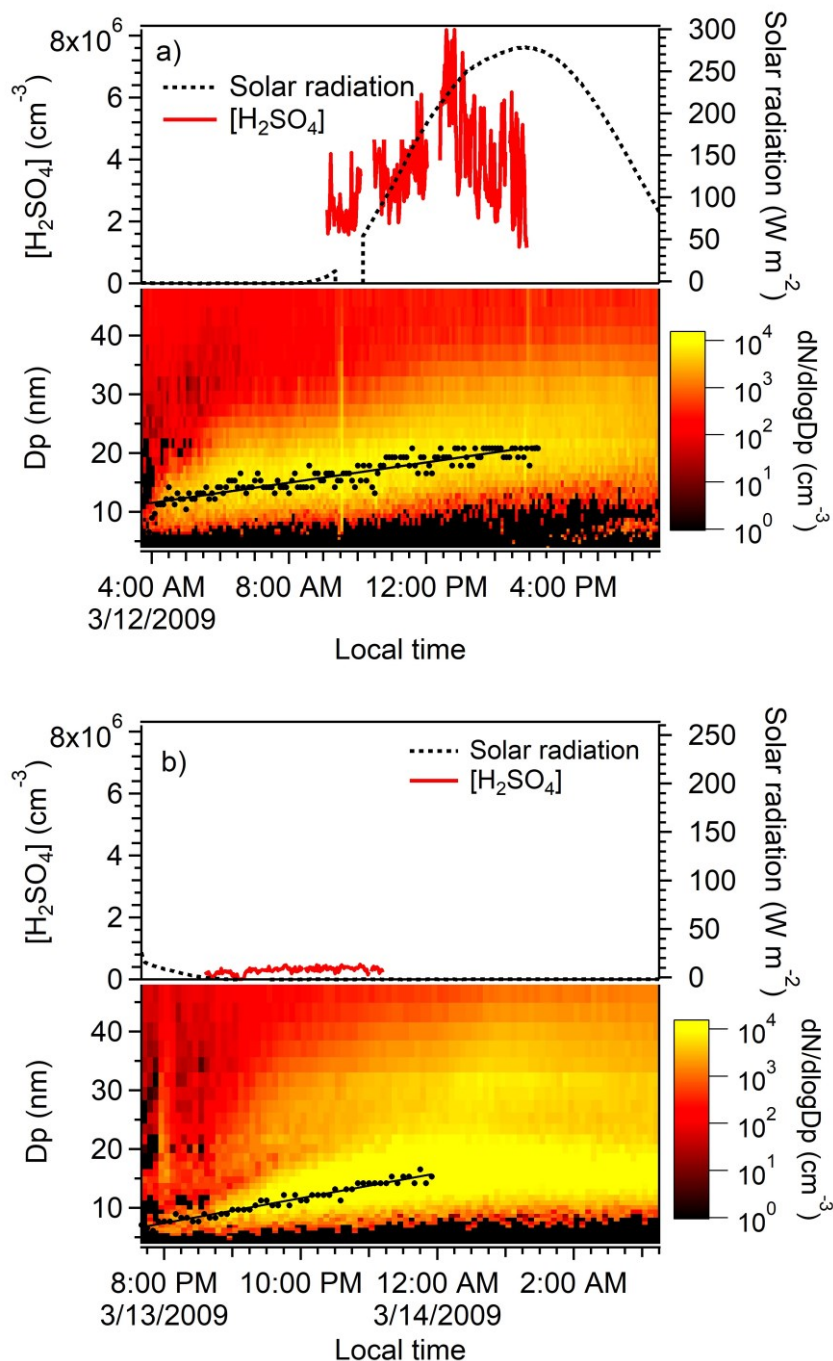


Figure 4. Photochemical and particle size distribution properties during ultrafine particle growth (a) Event 1 and (b) Event 2. Plotted are the gas-phase concentrations of H_2SO_4 (red, molecules cm^{-3}) and downwelling solar radiation (black dashes, $W m^{-2}$). Particle number size distributions for each growth event are shown with the mode diameter during the growth period and its linear regression fit to determine growth rates are shown in black.

351 ocean and atmosphere, and open ocean. Sea ice leads have been shown to contribute to sea spray and
 352 seawater-like particles in the atmosphere (May et al., 2016; Nilsson et al., 2001). The back trajectories for
 353 the air masses associated with both events originate in the same region of the Arctic Ocean, however there
 354 are differences in their geographic paths and altitudes. The air masses associated with Event 1 did not
 355 pass over the leads offshore of Prince Patrick Island (Northwest Territories, Canada) and spent more time

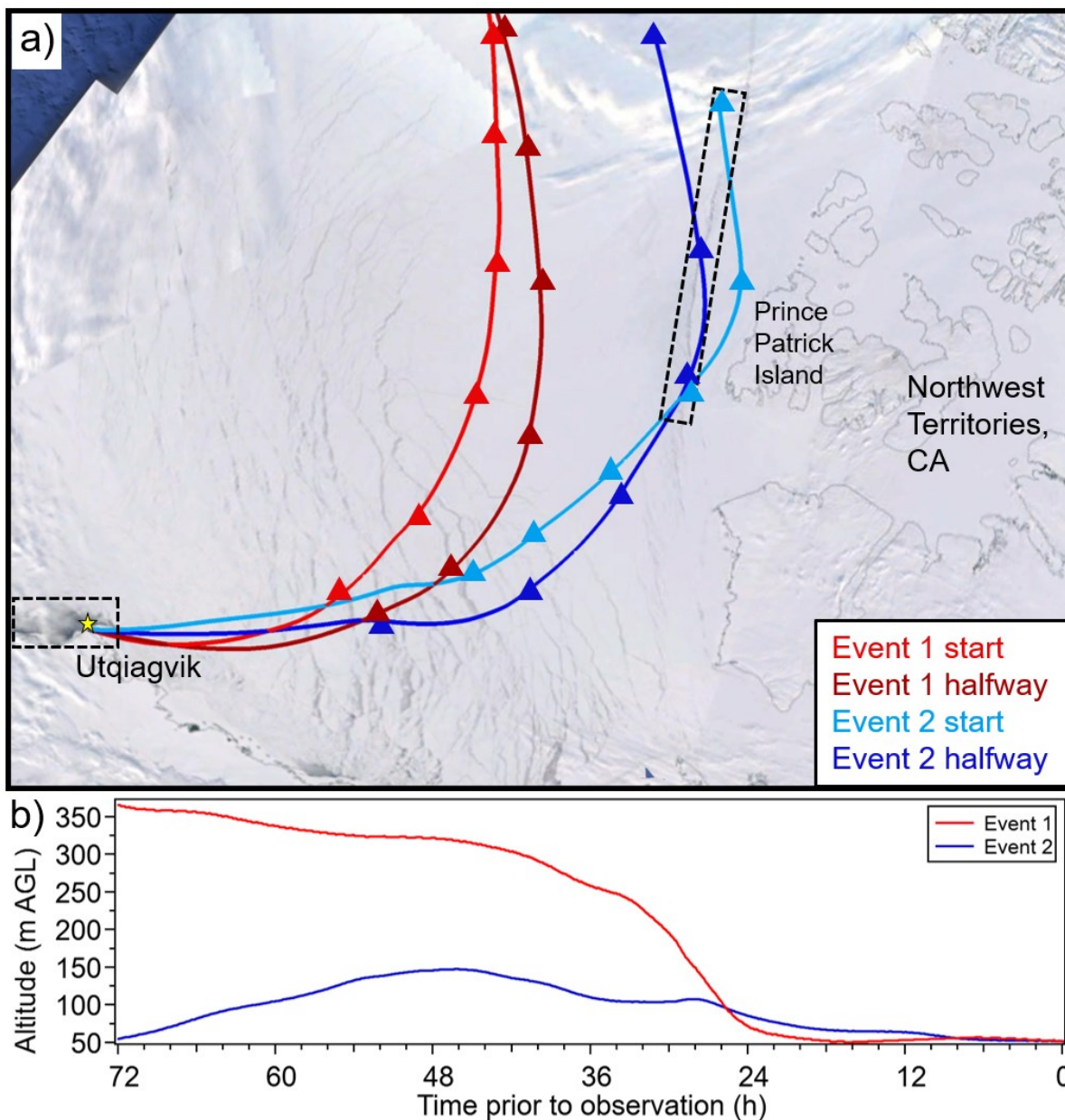


Figure 5. Air mass back trajectory analysis for each growth event. (a) HYSPLIT 72-hour back trajectories for each event plotted with MODIS satellite images from 3/11, with one trajectory at the beginning of each event and one halfway through growth. Triangles mark 12-hour time points. The blue region in the upper-left corner is an imaging artefact and does not represent open ocean. Black boxes highlight regions with sea ice leads. (b) Average altitudes above ground level (AGL) of the two trajectories calculated for each event.

356 aloft, at ~350 m above ground level (AGL) which near the top of the estimated boundary layer during this
357 time (Boylan et al., 2014), reaching surface level 24 hours before the start of the observed event. The air
358 masses impacting Event 2 passed over open leads off Prince Patrick Island and are much closer to the
359 surface (not exceeding 150 m AGL over the 72 hours), opening up the possibility that the source of the
360 species responsible for nucleation and/or growth came from these leads. Given the chemical complexity
361 of the marine upper boundary layer compared to near the surface (Zheng et al., 2021), the species
362 involved in particle growth are likely to be different for these two events.

363 While we have no direct measurements of wind speed at these open leads, measurements
364 performed at the measurement site provide some insights into the potential role of primary sea spray in
365 forming the initial seeds for condensational growth. When wind speeds exceed 4 m s^{-1} over open water,
366 breaking waves tend to produce sea spray aerosol (May et al., 2016; Nilsson et al., 2001). This
367 phenomenon has been previously observed at Utqiagvik in the winter in sub-500 nm particles (Kirpes et
368 al., 2018, 2019). During Event 1, the average wind speed recorded at the site was $5.3 \pm 0.9 \text{ m s}^{-1}$. Lower
369 wind speeds were measured during Event 2 (average of $2.2 \pm 0.2 \text{ m s}^{-1}$) but in both cases there was
370 turbulent ice flow offshore from the measurement site visible in the Barrow sea ice radar (Mahoney &
371 Jones, 2020), which has also been shown to form sea spray aerosol in the Arctic (Nilsson et al., 2001).

372 Using the SICIMS measurements, we estimated the contribution to the measured growth rate at
373 the measurement site from condensation of H_2SO_4 using the equation provided in Kuang et al. (2010) for
374 Γ , the fraction of growth that can be attributed to H_2SO_4 condensation:

$$375 \quad \Gamma = \frac{2GR_{meas}}{v_1[\text{H}_2\text{SO}_4]\bar{c}_1} \quad (4)$$

376 where GR_{meas} is the measured growth rate (nm h^{-1}), $[\text{H}_2\text{SO}_4]$ is the average number concentration of
377 H_2SO_4 measured onsite during the event (molecules cm^{-3}), v_1 is the volume of a hydrated H_2SO_4 molecule
378 ($1.7 \times 10^{-22} \text{ cm}^3$), and \bar{c}_1 is the mean thermal speed of the condensing H_2SO_4 monomer (nm hr^{-1}). From the
379 Γ calculations, the results of which are summarized in Table 1, we estimate that H_2SO_4 condensation
380 accounted for 22% of volumetric growth during Event 1 ($\Gamma = 4.5 \pm 1.5$) and did not contribute
381 substantially to Event 2 ($\Gamma = 139.2 \pm 4.2$). The Γ analysis assumes that the concentration of H_2SO_4
382 measured during each event represents that which sustained growth during the entire period of growth. It
383 thus assumes that the air mass is exposed to a constant supply of condensing H_2SO_4 and overlooks the role
384 of inhomogeneities during growth (Kivekäs et al., 2016). Nonetheless, the distinct differences in growth
385 rates and apparent influence from H_2SO_4 on observed particle growth are evidence of fundamental
386 differences in the species and circumstances responsible for the observed events. The SSA measured for

387 bulk aerosol during these events were very similar, suggesting the differences in these events were not
388 impacting larger particle radiative properties.

389

390 **Table 1.** Ultrafine particle growth rates and H₂SO₄ contribution to growth (Γ)

Event	T (°C)	GR _{meas} (nm h ⁻¹)	Γ	[H ₂ SO ₄] (cm ⁻³)
1 (12 March)	-26.4	0.862 ± 0.034	4.5 ± 1.5	3.7 × 10 ⁶
2 (13 – 14 March)	-27.6	2.12 ± 0.07	139.2 ± 4.2	3.0 × 10 ⁵

391

392 To further investigate the composition of the particles in each growth event, we next consider the
393 indirect measurements of UFP composition. Figure 6 shows 15 and 35 nm diameter *HGF* data for the two
394 events. An instrument malfunction resulted in missing 15 nm data during Event 1; that issue was resolved
395 midway through Event 2 but as a result we were only able to obtain one reliable measurement of 15 nm
396 *HGF* during that event. Based on the size distribution measurements shown in Figure 4, we postulate that
397 35 nm particle composition represents both background particles as well as those associated with the
398 growth events. While the condensing species are likely similar for both particle populations, prior studies
399 suggest a higher salt content in larger particles compared to smaller ones if these events began as primary
400 marine aerosol (Prather et al., 2013). Figure 6a shows both the average *HGF* distributions measured
401 during the growth events and the Gaussian fit to each distribution. The sampled particles in both growth
402 events were highly hygroscopic. The *HGF* for 35 nm diameter particles measured during Event 1 was
403 2.10 ± 0.10. *HGFs* of 15 nm and 35 nm diameter particles during Event 2 were 1.67 and 1.94 ± 0.07,
404 respectively. Measured *HGFs* of 35 nm particles are significantly higher than those measured during the
405 background period (Figure 2c), even compared to the period during 29 March when [H₂SO₄] was
406 similarly high. This difference is evidence of a compositional difference between the particles generated
407 in these two formation events and the background ultrafine particles at the site, and we hypothesize that
408 the former was highly influenced by primary marine particle production whereas the latter is more
409 representative of aged sulfate and organics as discussed above. The 35 nm *HGFs* measured for both
410 events are smaller than those previously reported for 50 nm mobility-selected sea salt particles (*HGF* =
411 2.3) (Zieger et al., 2017) but fall in the range of nebulized 40 nm sea water proxy with varying amounts of
412 organic material (*HGF* = 1.9 – 2.3, see Figure 2c) (Fuentes et al., 2011) and are larger than that of 35 nm

413 ammonium sulfate ($HGF = 1.65$) (Hämeri et al., 2000). Figure 6b shows that, during Event 1, 35 nm
 414 particle HGF slowly decreased from 2.20 to 1.95. Within measurement uncertainty, the HGF at the end
 415 of Event 1 corresponds to the average HGF measured during Event 2 (1.94 \pm 0.07), the latter of which
 416 remained relatively constant throughout its shorter 4-hour period of growth. The HGF distribution of 15
 417 nm particles sampled during Event 2 is narrower than those of 35 nm particles, which indicates that 15
 418 nm particles were compositionally more homogeneous compared to 35 nm particles. The peak HGF for

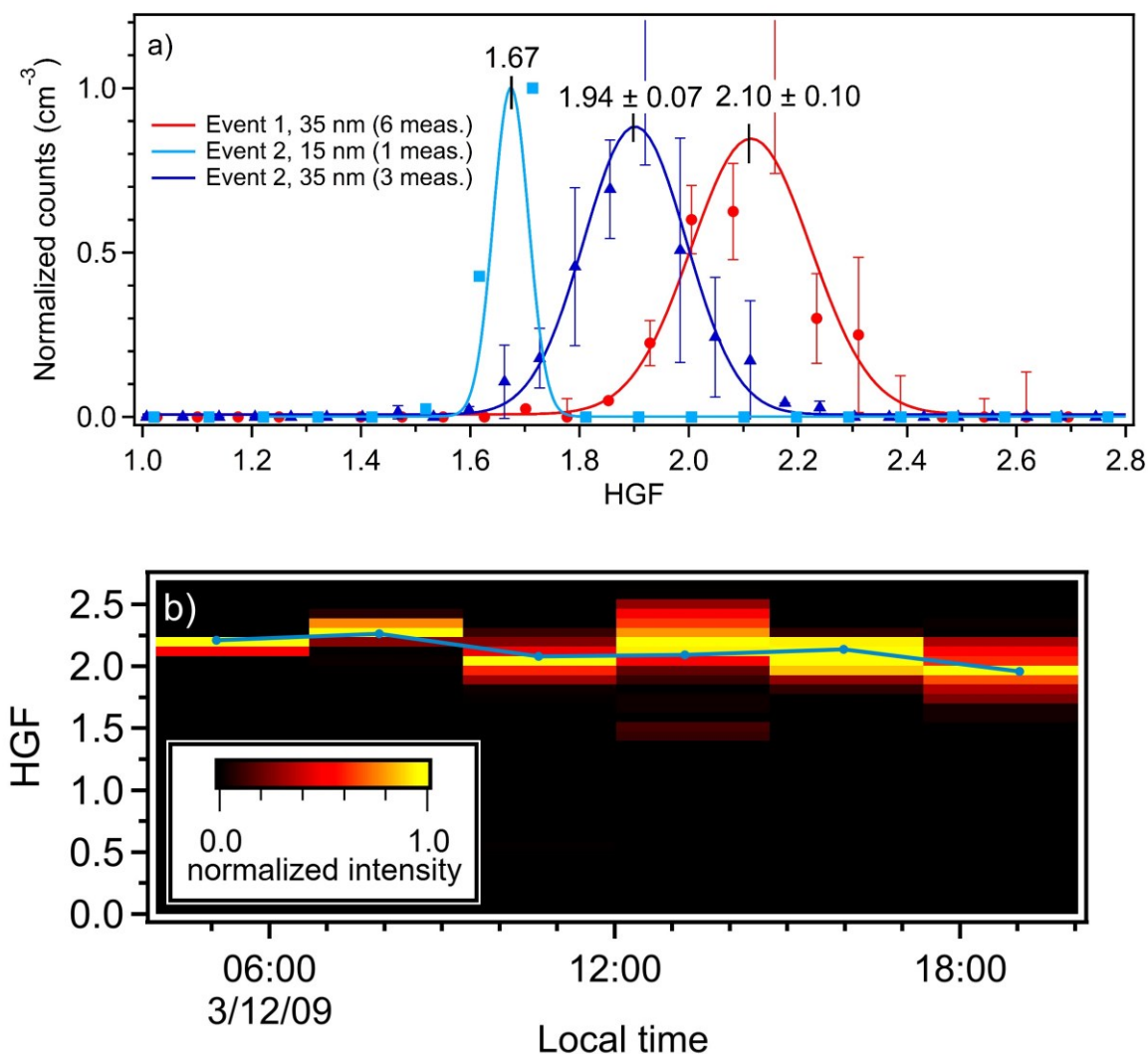


Figure 6. (a) Measured HGF s at 90% RH for 15 and 35 nm size-selected particles during each event (15 nm data missing for Event 1). Markers are the averaged size distributions measured during each event. The error bars represent standard deviation and the number of measurements at each size is shown in the legend. Solid lines are Gaussian fits of the data. Distributions were normalized prior to plotting to facilitate comparison. (b) Time evolution of Event 1 HGF . The Event 2 HGF distribution did not change during the growth period.

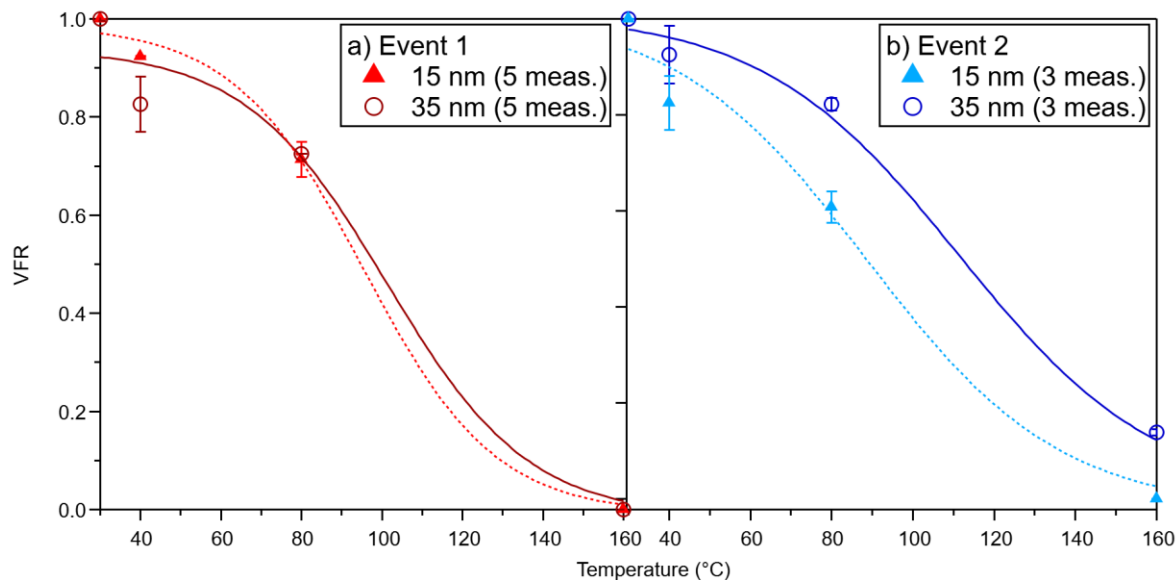


Figure 6. Volume fraction remaining at 40, 80, and 160 °C for 15 and 35 nm size-selected particles during (a) Event 1 and (b) Event 2. The error bars represent standard deviation and the number of measurements at each size is shown in the legend. Initial volume was assumed to be the volume at 30 °C.

419 15 nm particles, 1.67, is lower than that measured for 35 nm particles, in part due to the Kelvin effect but
 420 also likely because of the relatively smaller contribution of primary marine particle seeds to overall
 421 particle composition.

422 Figure 6 shows volatility measurements of 15 and 35 nm mobility-selected particles collected
 423 during the events. We note first that the *VFR* data are very similar for both particle sizes measured in
 424 Event 1, whereas Event 2 shows more substantial differences between the two sizes. One possible
 425 explanation for this can be seen in Figure 4, in which the size distribution of Event 1 (Figure 4a) appears
 426 to have a single mode and relatively low concentration of particles larger than 30 nm. In contrast, Event 2
 427 (Figure 4b) occurs with overall higher concentrations of particles larger than 30 nm in diameter.
 428 Considering the exceptionally high measured *HGF* measured during both events, it is likely that the
 429 differences in *VFR* during Event 2 arise from differences in the relative contributions of primary marine
 430 aerosol. In Event 1, 15 nm UFP volume is almost completely lost at 160 °C whereas, in Event 2, 15 nm
 431 particles appear to be somewhat less volatile. While generally it is true that background particles show
 432 similar volatility at 160 °C (see Figure 3), there is a notable difference in size-dependence of the *VFR* data
 433 from these events compared to that of the background period. For the latter, heating to 80 °C resulted in
 434 $19.2 \pm 0.2\%$ *VFR* for 35 nm particles, whereas during Event 1, *VFRs* of $71 \pm 4\%$ were measured for 15
 435 nm and $72.57 \pm 0.01\%$ 35 nm diameter particles. Event 2 showed a similar behavior, with *VFR* of 61 ± 3
 436 % for 15 nm particles and $82 \pm 1\%$ for 35 nm particles. Thus, compared to background particles, those

437 associated with these UFP formation events were significantly less volatile at 80 °C. We attribute this
438 difference in *VFR* at 80 °C to the relative contributions of organics and a low-volatility salt, which in the
439 case of the former is reported as ~40 % for laboratory-generated α -pinene SOA (Huffman et al., 2009)
440 and for the latter as ~100 % for ammonium sulfate and sodium chloride (Huffman et al., 2008; Villani et
441 al., 2007).

442 To summarize the observations of the two UFP growth events, both events display qualities of
443 regional new particle formation events, specifically sustained and continuous growth that persisted for
444 several hours. This suggests that particles formed over a large region and then were advected over the
445 measurement site, with the first particles detected corresponding to the least aged and the last ones the
446 most aged. Both events are characterized by higher *HGFs* than can be achieved by sulfate salts, and from
447 this we conclude that particles contained significant amounts of highly hygroscopic salts. These salts
448 typically have lower volatility than ammoniated sulfate. The high *HGF* measured are consistent with sea
449 salt consisting of NaCl and other trace elements, which is expected to be non-volatile at 160 °C (Mendes
450 et al., 2016; Villani et al., 2007). The non-volatile nature of NaCl was confirmed for 15 nm particles in
451 laboratory tests with our thermodenuder. Our measurements of 15 and 35 nm *VFR* at 80 °C are consistent
452 with published values for 25 nm *VFR* of marine nanoparticles sampled in Antarctica (Asmi et al., 2010)
453 and observations of 50 nm diameter particle volatility the Arctic and Pacific Oceans (Kim et al., 2015).
454 They are also consistent with reported 30-40 nm particle volatility performed in the North Atlantic (Quinn
455 et al., 2019) and coastal California (Bates et al., 2012), although those observations were performed at
456 higher temperatures (230 °C). Our observations of the importance of a component more hygroscopic than
457 ammonium sulfate in nanoparticle composition is inconsistent with the main conclusions of a study of
458 nanoparticle volatility performed at Svalbard by Giamarelou, et al. (2016), who concluded that
459 ammoniated sulfates dominated 12 nm particle composition. That study, which did not have supporting
460 hygroscopicity measurements nor direct measurements of sulfuric acid, based its conclusion on the
461 observation that ambient particles completely volatilized at 230 °C. The results for Event 2 are consistent
462 with a comprehensive study by Clarke et al., (2006), which concluded that marine UFPs contained a non-
463 volatile core with as much as 90 % by volume of a component that completely volatilized at 300 °C. We
464 hypothesize that the newly formed UFPs observed in this study are comprised of a mixture of volatile
465 organic species and a salt with hygroscopicity similar to sea salt or NaCl, but that largely volatilizes by
466 160 °C. We are not aware of any aerosol component that has this property but hope that future
467 observations can shed light on this intriguing property of newly formed particles in this region.

468 Our estimates of volume fraction based on the measured *HGFs* during these events are separated
 469 into the composition of 15 nm particles during Event 2, which minimizes potential biases from
 470 background particles and is therefore more representative of the species responsible for this event, and
 471 that of 35 nm particles during both events, which we hypothesize as being influenced by larger seed
 472 particles and higher levels of background particles. For the analysis of 35 nm particle composition, we
 473 consider a mixture of sea salt ($HGF = 2.2$), sulfuric acid ($HGF = 1.9$), and oxidized organic ($HGF = 1.2$).
 474 We acknowledge that our volatility observations may rule out sea salt but this is the only component that
 475 we are aware of that could be responsible for the high *HGFs* observed in this study and so we apply it to
 476 this analysis with the caveat that this component has this *HGF* but cannot be pure NaCl. Our Γ analysis
 477 (see Table 1) suggests that sulfuric acid may contribute to 22% of particulate volume during Event 1, and
 478 we use this information to constrain the contribution by sulfuric acid to composition during that event.
 479 For the analysis of 15 nm particle composition during Event 2, we use the following *HGFs* from prior
 480 studies: sea salt ($HGF = 2.0$) (Zieger et al., 2017) and oxidized organic ($HGF = 1.1$) (Virkkula et al.,
 481 1999). Table 2 summarizes the results of the analysis of these *HGF* measurements by the ZSR method.
 482 During both Events 1 and 2, 35 nm diameter particles contained significant amounts of the very
 483 hygroscopic “sea salt”, with an estimated volume fraction (ϵ_{SS}) of 0.74. The balance of composition is
 484 predominantly sulfuric acid for Event 1 ($\epsilon_{SA} = 0.22$), and oxidized organic for Event 2 ($\epsilon_{ORG} = 0.26$).
 485 Oxidized organics contributed a small amount to 35 nm particle composition in Event 1 ($\epsilon_{ORG} = 0.04$).
 486 Even though these results are based on measured *HGF*, they are qualitatively in agreement with the
 487 measurements of volatility if it were true that the oxidized organics were of low volatility. This possibility
 488 is also suggested in the study of Arctic aerosol volatility by Giamarelou et al. (2016). Finally, the
 489 significant contribution of “sea salt” to 35 nm particle composition in both events agrees qualitatively
 490 with the analyses of the size distribution, back trajectories and wind data, all of which point to the
 491 likelihood that marine emissions were responsible for the initiation of these events. As for the 15 nm
 492 diameter particles most associated with the UFP growth event, our analysis suggests that this event may
 493 have also begun with the formation of primary hygroscopic sea salt-like particles, and then subsequently

Table 2. Estimates of the volume fraction of representative compound classes during UFP formation events, based on analysis of *HGF* data using the ZSR mixing rule. ϵ_{SS} : volume fraction of hygroscopic sea salt, ϵ_{SA} : volume fraction of sulfuric acid, ϵ_{ORG} : volume fraction of organic compounds.

Event	Dp (nm)	ϵ_{SS}	ϵ_{SA}	ϵ_{ORG}
1 (12 March)	35	0.74	0.22	0.04
2 (13 – 14 March)	15	0.63	0	0.37
	35	0.74	0	0.26

494 grew from the condensation of organic compounds. As mentioned previously, Event 2 was first observed
495 at the site with a measured modal diameter of 7 nm, so while this qualitatively agrees with the *HGF*
496 measurements that suggest a sea salt-like core, the *HGF* measurements suggest a much higher volume
497 fraction.

498
499

500 **4 Conclusion**

501 In this manuscript, we report indirect composition measurements of ultrafine particles in
502 Utqiagvik, Alaska, observed during late winter and early spring (5 March – 14 April 2009). Our estimates
503 of size-resolved particle composition combine measurements of particle hygroscopicity and volatility
504 with those of gas-phase H₂SO₄. During “background” periods with minimal local anthropogenic
505 influence, ultrafine particles in this region were characterized by low concentrations, especially sub-20
506 nm diameter particles. Under these conditions, particles exhibited moderate hygroscopic growth that
507 suggests a mixed organic-inorganic composition. Volatility measurements support this observation, with
508 less than 20% *VFR* measured for sub-100 nm particles. We estimated the volume fractions of
509 representative compounds using the ZSR method and found that ammoniated sulfate (~30% by volume)
510 and low-hygroscopicity oxidized organics (~70% by volume) could account for the measured
511 hygroscopicity of 35 nm particles. Gas-phase H₂SO₄ generally trends with solar radiation but did not
512 follow a regular diurnal pattern in this campaign. We also analyzed two ultrafine particle growth events
513 wherein the properties of the particles differed greatly from those measured during the background
514 period. Both growth events produced highly hygroscopic particles, but the differences in the average
515 measured hygroscopic growth factors (Event 1: 2.1; Event 2: 1.9), as well as growth rates and H₂SO₄
516 contributions to growth, suggest differences in their chemical composition. HYSPLIT back trajectories
517 and MODIS satellite imagery suggest that Event 1 was likely influenced by upper marine boundary layer
518 processes, while Event 2 passed over open leads in the lower boundary layer. Both hygroscopicity and
519 volatility data show that particles in both growth events contain a significant volume fraction of high
520 hygroscopicity, low volatility species and support a role for primary marine emissions similar to sea salt
521 as the initial seed for these events. The preponderance of evidence suggests that Event 1 particles were
522 composed of mixtures of sea salt-like species and sulfuric acid, whereas Event 2 particles contained
523 similar levels of salt but the balance of the composition was oxidized organics. This sea salt-like species,
524 which is highly hygroscopic but more volatile than NaCl, is not known and illustrates the necessity of
525 further measurements in this region. This study illuminates the importance of a multi-pronged approach to
526 indirect measurements of ultrafine particle composition and illustrates the variability that exists between
527 background aerosol and newly formed aerosol. It also highlights to potentially important role of low-

528 volatility, high-hygroscopicity primary marine species like sea salt as initiators of ultrafine particle
529 production in the Arctic late-winter. Additional measurements during this understudied time of year
530 should be performed to better elucidate the processes driving particle production in this important region.

531

532 **Acknowledgement**

533 The authors wish to thank the organizers of the OASIS 2009 field campaign, the Barrow Arctic Science
534 Consortium for logistics support, and all of the researchers who contributed to the campaign. The authors
535 gratefully acknowledge funding for the analysis of this dataset by the Department of Energy, grant DE-
536 SC0019000. All data from the OASIS Barrow 2009 field campaign are publicly available at
537 10.5065/D6CJ8BM3.

538

539

540 **Citations**

541 Abbatt, J. P. D., Leaitch, W. R., Aliabadi, A. A., Bertram, A. K., Blanchet, J.-P., Boivin-Rioux, A., et al.
542 (2019). Overview paper: New insights into aerosol and climate in the Arctic. *Atmospheric Chemistry*
543 *and Physics*, 19. <https://doi.org/10.5194/acp-19-2527-2019>

544 Allan, J. D., Williams, P. I., Najera, J., Whitehead, J. D., Flynn, M. J., Taylor, J. W., et al. (2015). Iodine
545 observed in new particle formation events in the Arctic atmosphere during ACCACIA. *Atmospheric*
546 *Chemistry and Physics*, 15(10), 5599–5609. <https://doi.org/10.5194/acp-15-5599-2015>

547 Asmi, E., Frey, A., Virkkula, A., Ehn, M., Manninen, H. E., Timonen, H., et al. (2010). Hygroscopicity
548 and chemical composition of Antarctic sub-micrometre aerosol particles and observations of new
549 particle formation. *Atmospheric Chemistry and Physics*, 10, 4253–4271. [https://doi.org/10.5194/acp-](https://doi.org/10.5194/acp-10-4253-2010)
550 10-4253-2010

551 Asmi, E., Kondratyev, V., Brus, D., Laurila, T., Lihavainen, H., Backman, J., et al. (2016). Aerosol size
552 distribution seasonal characteristics measured in Tiksi, Russian Arctic. *Atmospheric Chemistry and*
553 *Physics*, 16(3), 1271–1287. <https://doi.org/10.5194/acp-16-1271-2016>

554 Baccarini, A., Karlsson, L., Dommen, J., Duplessis, P., Vüllers, J., Brooks, I. M., et al. (2020). Frequent
555 new particle formation over the high Arctic pack ice by enhanced iodine emissions. *Nature*
556 *Communications*, 11(1). <https://doi.org/10.1038/s41467-020-18551-0>

557 Barrie, L. A. (1986). Arctic air pollution: An overview of current knowledge. *Atmospheric Environment*,
558 20(4), 643–663. [https://doi.org/10.1016/0004-6981\(86\)90180-0](https://doi.org/10.1016/0004-6981(86)90180-0)

559 Bates, T. S., Quinn, P. K., Frossard, A. A., Russell, L. M., Hakala, J., Petäjä, T., et al. (2012).
560 Measurements of ocean derived aerosol off the coast of California. *Journal of Geophysical Research*
561 *Atmospheres*, 117(12), 0–15. <https://doi.org/10.1029/2012JD017588>

562 Bergin, M. H., Ogren, J. A., Schwartz, S. E., & McInnes, L. M. (1997). Evaporation of ammonium nitrate
563 aerosol in a heated nephelometer: Implications for field measurements. *Environmental Science and*
564 *Technology*, 31(10), 2878–2883. <https://doi.org/10.1021/es970089h>

565 Bodhaine, B. A., Harris, J. M., & Herbert, G. A. (1981). Aerosol light scattering and condensation nuclei
566 measurements at Barrow, Alaska. *Atmospheric Environment*, 15(8), 1375–1389.

- 567 [https://doi.org/10.1016/0004-6981\(81\)90344-9](https://doi.org/10.1016/0004-6981(81)90344-9)
- 568 Boylan, P., Helmig, D., Staebler, R., Turnipseed, A., Fairall, C., & Neff, W. (2014). Boundary layer
569 dynamics during the Ocean-Atmosphere-Sea-Ice-Snow (OASIS) 2009 experiment at Barrow, AK.
570 *Journal of Geophysical Research: Atmospheres*, *119*(5), 2261–2278.
571 <https://doi.org/10.1002/2013JD020299>
- 572 Browse, J., Carslaw, K. S., Arnold, S. R., Pringle, K., & Boucher, O. (2012). The scavenging processes
573 controlling the seasonal cycle in Arctic sulphate and black carbon aerosol. *Atmospheric Chemistry
574 and Physics*, *12*(15), 6775–6798. <https://doi.org/10.5194/acp-12-6775-2012>
- 575 Burkart, J., Hodshire, A. L., Mungall, E. L., Pierce, J. R., Collins, D. B., Ladino, L. A., et al. (2017).
576 Organic Condensation and Particle Growth to CCN Sizes in the Summertime Marine Arctic Is
577 Driven by Materials More Semivolatile Than at Continental Sites. *Geophysical Research Letters*,
578 *44*(20), 10,725-10,734. <https://doi.org/10.1002/2017GL075671>
- 579 Burtscher, H., Baltensperger, U., Bukowiecki, N., Cohn, P., Hüglin, C., Mohr, M., et al. (2001).
580 Separation of volatile and non-volatile aerosol fractions by thermodesorption: Instrumental
581 development and applications. *Journal of Aerosol Science*, *32*(4), 427–442.
582 [https://doi.org/10.1016/S0021-8502\(00\)00089-6](https://doi.org/10.1016/S0021-8502(00)00089-6)
- 583 Chang, R. Y. W., Sjostedt, S. J., Pierce, J. R., Papakyriakou, T. N., Scarratt, M. G., Michaud, S., et al.
584 (2011). Relating atmospheric and oceanic DMS levels to particle nucleation events in the Canadian
585 Arctic. *Journal of Geophysical Research Atmospheres*, *116*(21).
586 <https://doi.org/10.1029/2011JD015926>
- 587 Clarke, A. D., Charlson, R. J., & Radke, L. F. (1984). Airborne observations of Arctic aerosol, IV:
588 Optical properties of Arctic haze. *Geophysical Research Letters*, *11*(5).
589 <https://doi.org/10.1029/GL011i005p00405>
- 590 Clarke, A. D., Owens, S. R., & Zhou, J. (2006). An ultrafine sea-salt flux from breaking waves:
591 Implications for cloud condensation nuclei in the remote marine atmosphere. *Journal of
592 Geophysical Research*, *111*(D6), D06202. <https://doi.org/10.1029/2005JD006565>
- 593 Cochran, R. E., Ryder, O. S., Grassian, V. H., & Prather, K. A. (2017). Sea spray aerosol: The chemical
594 link between the oceans, atmosphere, and climate. *Accounts of Chemical Research*. American
595 Chemical Society. <https://doi.org/10.1021/acs.accounts.6b00603>
- 596 Collins, D. B., Burkart, J., Y-W Chang, R., Lizotte, M., Boivin-Rioux, A., Blais, M., et al. (2017).
597 Frequent ultrafine particle formation and growth in Canadian Arctic marine and coastal
598 environments. *Atmospheric Chemistry and Physics*, *17*, 13119–13138. <https://doi.org/10.5194/acp-17-13119-2017>
- 600 Covert, D. S., & Heintzenberg, J. (1993). Size distributions and chemical properties of aerosol at Ny
601 Ålesund, Svalbard. *Atmospheric Environment Part A, General Topics*, *27*(17–18), 2989–2997.
602 [https://doi.org/10.1016/0960-1686\(93\)90331-R](https://doi.org/10.1016/0960-1686(93)90331-R)
- 603 Croft, B., Martin, R. V., Leaitch, W. R., Tunved, P., Breider, T. J., D’Andrea, S. D., & Pierce, J. R.
604 (2016). Processes controlling the annual cycle of Arctic aerosol number and size distributions.
605 *Atmospheric Chemistry and Physics*, *16*, 3665–3682. <https://doi.org/10.5194/acp-16-3665-2016>
- 606 Croft, B., Martin, R. V., Richard Leaitch, W., Burkart, J., Y-W Chang, R., Collins, D. B., et al. (2019).
607 Arctic marine secondary organic aerosol contributes significantly to summertime particle size
608 distributions in the Canadian Arctic Archipelago. *Atmospheric Chemistry and Physics*, *19*, 2787–
609 2812. <https://doi.org/10.5194/acp-19-2787-2019>

- 610 Dal Maso, M., Kulmala, M., Riipinen, I., Wagner, R., Hussein, T., Aalto, P. P., & Lehtinen, K. E. J.
611 (2005). Formation and growth of fresh atmospheric aerosols: Eight years of aerosol size distribution
612 data from SMEAR II, Hyytiälä, Finland. *Boreal Environment Research*, 10(5), 323–336.
- 613 Dall’Osto, M., Beddows, D. C. S., Tunved, P., Krejci, R., Ström, J., Hansson, H. C., et al. (2017). Arctic
614 sea ice melt leads to atmospheric new particle formation. *Scientific Reports*, 7(1), 1–10.
615 <https://doi.org/10.1038/s41598-017-03328-1>
- 616 Dall’Osto, M., Simo, R., Harrison, R. M., Beddows, D. C. S., Saiz-Lopez, A., Lange, R., et al. (2018).
617 Abiotic and biotic sources influencing spring new particle formation in North East Greenland.
618 *Atmospheric Environment*, 190, 126–134. <https://doi.org/10.1016/j.atmosenv.2018.07.019>
- 619 Dall’Osto, M., Geels, C., Beddows, D. C. S., Boertmann, D., Lange, R., Nøjgaard, J. K., et al. (2018).
620 Regions of open water and melting sea ice drive new particle formation in North East Greenland.
621 *Scientific Reports*, 8(1), 1–10. <https://doi.org/10.1038/s41598-018-24426-8>
- 622 Ferek, R. J., Hobbs, P. V., Radke, L. F., Herring, J. A., Sturges, W. T., & Cota, G. F. (1995). Dimethyl
623 sulfide in the Arctic atmosphere. *Journal of Geophysical Research*, 100(D12), 26093–26104.
624 <https://doi.org/10.1029/95jd02374>
- 625 Flowers, B. A., Dubey, M. K., Mazzoleni, C., Stone, E. A., Schauer, J. J., Kim, S. W., & Yoon, S. C.
626 (2010). Optical-chemical-microphysical relationships and closure studies for mixed carbonaceous
627 aerosols observed at Jeju Island; 3-laser photoacoustic spectrometer, particle sizing, and filter
628 analysis. *Atmospheric Chemistry and Physics*, 10(21), 10387–10398. [https://doi.org/10.5194/acp-10-](https://doi.org/10.5194/acp-10-10387-2010)
629 [10387-2010](https://doi.org/10.5194/acp-10-10387-2010)
- 630 Frieß, U., Sihler, H., Sander, R., Phler, D., Yilmaz, S., & Platt, U. (2011). The vertical distribution of BrO
631 and aerosols in the Arctic: Measurements by active and passive differential optical absorption
632 spectroscopy. *Journal of Geophysical Research Atmospheres*, 116(18).
633 <https://doi.org/10.1029/2011JD015938>
- 634 Frossard, A. A., Shaw, P. M., Russell, L. M., Kroll, J. H., Canagaratna, M. R., Worsnop, D. R., et al.
635 (2011). Springtime Arctic haze contributions of submicron organic particles from European and
636 Asian combustion sources. *Journal of Geophysical Research-Atmospheres*, 116.
637 <https://doi.org/10.1029/2010jd015178>
- 638 Frossard, A. A., Russell, L. M., Massoli, P., Bates, T. S., & Quinn, P. K. (2014). Side-by-side comparison
639 of four techniques explains the apparent differences in the organic composition of generated and
640 ambient marine aerosol particles. *Aerosol Science and Technology*, 48(3), v–x.
641 <https://doi.org/10.1080/02786826.2013.879979>
- 642 Fuentes, E., Coe, H., Green, D., & McFiggans, G. (2011). On the impacts of phytoplankton-derived
643 organic matter on the properties of the primary marine aerosol - Part 2: Composition, hygroscopicity
644 and cloud condensation activity. *Atmospheric Chemistry and Physics*, 11(6), 2585–2602.
645 <https://doi.org/10.5194/acp-11-2585-2011>
- 646 Garrett, T. J., Brattström, S., Sharma, S., Worthy, D. E. J., & Novelli, P. (2011). The role of scavenging in
647 the seasonal transport of black carbon and sulfate to the Arctic. *Geophysical Research Letters*,
648 38(16). <https://doi.org/10.1029/2011GL048221>
- 649 Ghahremaninezhad, R., Norman, A.-L., Abbatt, J. P. D., Lévassieur, M., & Thomas, J. L. (2016).
650 Biogenic, anthropogenic and sea salt sulfate size-segregated aerosols in the Arctic summer.
651 *Atmospheric Chemistry and Physics*, 16(8), 5191–5202. <https://doi.org/10.5194/acp-16-5191-2016>
- 652 Giamarelou, M., Eleftheriadis, K., Nyeki, S., Tunved, P., Torseth, K., & Biskos, G. (2016). Indirect

- 653 evidence of the composition of nucleation mode atmospheric particles in the high Arctic. *Journal of*
654 *Geophysical Research: Atmospheres*, 121(2), 965–975. <https://doi.org/10.1002/2015JD023646>
- 655 Gysel, M., Weingartner, E., Nyeki, S., Paulsen, D., Baltensperger, U., Galambos, I., & Kiss, G. (2004).
656 Hygroscopic properties of water-soluble matter and humic-like organics in atmospheric fine aerosol.
657 *Atmospheric Chemistry and Physics*, 4(1), 35–50. <https://doi.org/10.5194/acp-4-35-2004>
- 658 Gysel, M., McFiggans, G. B., & Coe, H. (2009). Inversion of tandem differential mobility analyser
659 (TDMA) measurements. *Journal of Aerosol Science*, 40(2).
660 <https://doi.org/10.1016/j.jaerosci.2008.07.013>
- 661 Häkkinen, S. A. K., Äijälä, M., Lehtipalo, K., Junninen, H., Backman, J., Virkkula, A., et al. (2012).
662 Long-term volatility measurements of submicron atmospheric aerosol in Hyytiälä, Finland.
663 *Atmospheric Chemistry and Physics*, 12(22), 10771–10786. [https://doi.org/10.5194/acp-12-10771-](https://doi.org/10.5194/acp-12-10771-2012)
664 2012
- 665 Hall, D. K., & Riggs, G. A. (2015). MODIS/Aqua Sea Ice Extent 5-Min L2 Swath 1km, Version 6
666 [March 2009]. Retrieved February 18, 2021, from <https://doi.org/10.5067/MODIS/MYD29.006>
- 667 Hämeri, K., Väkevä, M., Hansson, H.-C., & Laaksonen, A. (2000). Hygroscopic growth of ultrafine
668 ammonium sulphate aerosol measured using an ultrafine tandem differential mobility analyzer.
669 *Journal of Geophysical Research: Atmospheres*, 105(D17), 22231–22242.
670 <https://doi.org/10.1029/2000JD900220>
- 671 Hawkins, L. N., & Russell, L. M. (2010). Polysaccharides, Proteins, and Phytoplankton Fragments: Four
672 Chemically Distinct Types of Marine Primary Organic Aerosol Classified by Single Particle
673 Spectromicroscopy. *Advances in Meteorology*, 2010, 1–14. <https://doi.org/10.1155/2010/612132>
- 674 Heintzenberg, J. (1982). Size-segregated measurements of particulate elemental carbon and aerosol light
675 absorption at remote arctic locations. *Atmospheric Environment (1967)*, 16(10), 2461–2469.
676 [https://doi.org/10.1016/0004-6981\(82\)90136-6](https://doi.org/10.1016/0004-6981(82)90136-6)
- 677 Heintzenberg, J., Leck, C., & Tunved, P. (2015). Potential source regions and processes of aerosol in the
678 summer Arctic. *Atmospheric Chemistry and Physics*, 15, 6487–6502. [https://doi.org/10.5194/acp-](https://doi.org/10.5194/acp-15-6487-2015)
679 15-6487-2015
- 680 Hinds, William C. (1999). *Aerosol Technology: Properties, Behavior, and Measurement of Airborne*
681 *Particles*, 2nd Edition | Wiley. Retrieved May 17, 2021, from [https://www.wiley.com/en-](https://www.wiley.com/en-us/Aerosol+Technology%3A+Properties%2C+Behavior%2C+and+Measurement+of+Airborne+Particles%2C+2nd+Edition-p-9780471194101)
682 [us/Aerosol+Technology%3A+Properties%2C+Behavior%2C+and+Measurement+of+Airborne+Part](https://www.wiley.com/en-us/Aerosol+Technology%3A+Properties%2C+Behavior%2C+and+Measurement+of+Airborne+Particles%2C+2nd+Edition-p-9780471194101)
683 [icles%2C+2nd+Edition-p-9780471194101](https://www.wiley.com/en-us/Aerosol+Technology%3A+Properties%2C+Behavior%2C+and+Measurement+of+Airborne+Particles%2C+2nd+Edition-p-9780471194101)
- 684 Huffman, J. A., Ziemann, P. J., Jayne, J. T., Worsnop, D. R., & Jimenez, J. L. (2008). Development and
685 Characterization of a Fast-Stepping/Scanning Thermodesorber for Chemically-Resolved Aerosol
686 Volatility Measurements. *Aerosol Science and Technology*, 42(5), 395–407.
687 <https://doi.org/10.1080/02786820802104981>
- 688 Huffman, J. A., Docherty, K. S., Mohr, C., Cubison, M. J., Ulbrich, I. M., Ziemann, P. J., et al. (2009).
689 Chemically-resolved volatility measurements of organic aerosol from different sources.
690 *Environmental Science and Technology*, 43(14), 5351–5357. <https://doi.org/10.1021/es803539d>
- 691 Jennings, S. G., O’Dowd, C. D., Cooke, W. F., Sheridan, P. J., & Cachier, H. (1994). Volatility of
692 elemental carbon. *Geophysical Research Letters*, 21(16), 1719–1722.
693 <https://doi.org/10.1029/94GL01423>
- 694 Karl, M., Leck, C., Gross, A., & Pirjola, L. (2012). A study of new particle formation in the marine
695 boundary layer over the central Arctic Ocean using a flexible multicomponent aerosol dynamic

- 696 model. *Tellus B: Chemical and Physical Meteorology*, 64(1).
 697 <https://doi.org/10.3402/tellusb.v64i0.17158>
- 698 Karl, M., Leck, C., Coz, E., & Heintzenberg, J. (2013). Marine nanogels as a source of atmospheric
 699 nanoparticles in the high Arctic. *Geophysical Research Letters*, 40(14), 3738–3743.
 700 <https://doi.org/10.1002/grl.50661>
- 701 Kecorius, S., Vogl, T., Paasonen, P., Lampilahti, J., Rothenberg, D., Wex, H., et al. (2019). New particle
 702 formation and its effect on cloud condensation nuclei abundance in the summer Arctic: a case study
 703 in the Fram Strait and Barents Sea. *Atmospheric Chemistry and Physics*, 19(22), 14339–14364.
 704 <https://doi.org/10.5194/acp-19-14339-2019>
- 705 Keith, C. H., & Arons, A. B. (1954). The Growth of Sea-Salt Particles by Condensation of Atmospheric
 706 Water Vapor. *Journal of Meteorology*, 11(3). [https://doi.org/10.1175/1520-
 707 0469\(1954\)011<0173:TGOSSP>2.0.CO;2](https://doi.org/10.1175/1520-0469(1954)011<0173:TGOSSP>2.0.CO;2)
- 708 Kim, G., Cho, H., Seo, A., Kim, D., Gim, Y., Yong Lee, B., et al. (2015). Comparison of Hygroscopicity,
 709 Volatility, and Mixing State of Submicrometer Particles between Cruises over the Arctic Ocean and
 710 the Pacific Ocean. *Environmental Science and Technology*, 49, 51.
 711 <https://doi.org/10.1021/acs.est.5b01505>
- 712 Kirpes, R. M., Bondy, A. L., Bonanno, D., Moffet, R. C., Wang, B., Laskin, A., et al. (2018). Secondary
 713 sulfate is internally mixed with sea spray aerosol and organic aerosol in the winter Arctic.
 714 *Atmospheric Chemistry and Physics*, 18(6), 3937–3949. <https://doi.org/10.5194/acp-18-3937-2018>
- 715 Kirpes, R. M., Bonanno, D., May, N. W., Fraund, M., Barget, A. J., Moffet, R. C., et al. (2019a).
 716 Wintertime Arctic Sea Spray Aerosol Composition Controlled by Sea Ice Lead Microbiology. *ACS*
 717 *Central Science*, 5(11), 1760–1767. <https://doi.org/10.1021/acscentsci.9b00541>
- 718 Kirpes, R. M., Bonanno, D., May, N. W., Fraund, M., Barget, A. J., Moffet, R. C., et al. (2019b).
 719 Wintertime Arctic Sea Spray Aerosol Composition Controlled by Sea Ice Lead Microbiology. *ACS*
 720 *Central Science*, 5(11), 1760–1767. <https://doi.org/10.1021/acscentsci.9b00541>
- 721 Kivekäs, N., Carpmann, J., Roldin, P., Leppä, J., O'Connor, E., Kristensson, A., & Asmi, E. (2016).
 722 Coupling an aerosol box model with one-dimensional flow: a tool for understanding observations of
 723 new particle formation events. *Tellus B: Chemical and Physical Meteorology*, 68(1), 29706.
 724 <https://doi.org/10.3402/tellusb.v68.29706>
- 725 Kolesar, K. R., Cellini, J., Peterson, P. K., Jefferson, A., Tuch, T., Birmili, W., et al. (2017). Effect of
 726 Prudhoe Bay emissions on atmospheric aerosol growth events observed in Utqiagvik (Barrow),
 727 Alaska. *Atmospheric Environment*, 152, 146–155. <https://doi.org/10.1016/j.atmosenv.2016.12.019>
- 728 Kreidenweis, S. M., McInnes, L. M., & Brechtel, F. J. (1998). Observations of aerosol volatility and
 729 elemental composition at Macquarie Island during the First Aerosol Characterization Experiment
 730 (ACE 1). *Journal of Geophysical Research: Atmospheres*, 103(D13), 16511–16524.
 731 <https://doi.org/10.1029/98JD00800>
- 732 Kuang, C., Riipinen, I., Sihto, S.-L., Kulmala, M., McCormick, A. V., & McMurry, P. H. (2010). An
 733 improved criterion for new particle formation in diverse atmospheric environments. *Atmospheric*
 734 *Chemistry and Physics*, 10(17), 8469–8480. <https://doi.org/10.5194/acp-10-8469-2010>
- 735 Kupiszewski, P., Leck, C., Tjernström, M., Sjogren, S., Sedlar, J., Graus, M., et al. (2013). Vertical
 736 profiling of aerosol particles and trace gases over the central Arctic Ocean during summer.
 737 *Atmospheric Chemistry and Physics*, 13(24), 12405–12431. [https://doi.org/10.5194/acp-13-12405-
 738 2013](https://doi.org/10.5194/acp-13-12405-2013)

- 739 Lance, S., Raatikainen, T., Onasch, T. B., Worsnop, D. R., Yu, X. Y., Alexander, M. L., et al. (2013).
740 Aerosol mixing state, hygroscopic growth and cloud activation efficiency during MIRAGE 2006.
741 *Atmospheric Chemistry and Physics*, 13(9), 5049–5062. <https://doi.org/10.5194/acp-13-5049-2013>
- 742 Law, K. S., & Stohl, A. (2007, March 16). Arctic air pollution: Origins and impacts. *Science*. American
743 Association for the Advancement of Science. <https://doi.org/10.1126/science.1137695>
- 744 Leaitch, W. R., Sharma, S., Huang, L., Toom-Sauntry, D., Chivulescu, A., Macdonald, A. M., et al.
745 (2013). Dimethyl sulfide control of the clean summertime Arctic aerosol and cloud. *Elementa:
746 Science of the Anthropocene*, 1(0), 000017. <https://doi.org/10.12952/journal.elementa.000017>
- 747 Leck, C, Gao, Q., Mashayekhy Rad, F., & Nilsson, U. (2013). Atmospheric Chemistry and Physics Size-
748 resolved atmospheric particulate polysaccharides in the high summer Arctic. *Atmospheric Chemistry
749 and Physics*, 13, 12573–12588. <https://doi.org/10.5194/acp-13-12573-2013>
- 750 Leck, Caroline, & Bigg, E. K. (2010). New Particle Formation of Marine Biological Origin. *Aerosol
751 Science and Technology*, 44(7), 570–577. <https://doi.org/10.1080/02786826.2010.481222>
- 752 Liao, J., Huey, L. G., Tanner, D. J., Flocke, F. M., Orlando, J. J., Neuman, J. A., et al. (2012).
753 Observations of inorganic bromine (HOBr, BrO, and Br₂) speciation at Barrow, Alaska, in spring
754 2009. *Journal of Geophysical Research: Atmospheres*, 117(D14).
755 [https://doi.org/10.1029/2011JD016641@10.1002/\(ISSN\)2169-8996.OASIS1](https://doi.org/10.1029/2011JD016641@10.1002/(ISSN)2169-8996.OASIS1)
- 756 Malm, W. C., & Kreidenweis, S. M. (1997). The effects of models of aerosol hygroscopicity on the
757 apportionment of extinction. *Atmospheric Environment*, 31(13), 1965–1976.
758 [https://doi.org/10.1016/S1352-2310\(96\)00355-X](https://doi.org/10.1016/S1352-2310(96)00355-X)
- 759 Mauldin, R. L., Frost, G. J., Chen, G., Tanner, D. J., Prevot, A. S. H., Davis, D. D., & Eisele, F. L.
760 (1998). OH measurements during the First Aerosol Characterization Experiment (ACE 1):
761 Observations and model comparisons. *Journal of Geophysical Research: Atmospheres*, 103(D13),
762 16713–16729. <https://doi.org/10.1029/98JD00882>
- 763 May, N. W., Quinn, P. K., McNamara, S. M., & Pratt, K. A. (2016). Multiyear study of the dependence of
764 sea salt aerosol on wind speed and sea ice conditions in the coastal Arctic. *Journal of Geophysical
765 Research: Atmospheres*, 121(15), 9208–9219. <https://doi.org/10.1002/2016JD025273>
- 766 Mendes, L., Eleftheriadis, K., & Biskos, G. (2016). Performance comparison of two thermodenuders in
767 Volatility Tandem DMA measurements. *Journal of Aerosol Science*, 92, 38–52.
768 <https://doi.org/10.1016/j.jaerosci.2015.10.002>
- 769 NCAR. (2012). Location information and pictures of the OASIS Barrow field intensive Spring 2009.
770 Retrieved February 3, 2021, from <https://data.eol.ucar.edu/dataset/106.366>
- 771 Nguyen, Q. T., Glasius, M., Sørensen, L. L., Jensen, B., Skov, H., Birmili, W., et al. (2016). Seasonal
772 variation of atmospheric particle number concentrations, new particle formation and atmospheric
773 oxidation capacity at the high Arctic site Villum Research Station, Station Nord. *Atmospheric
774 Chemistry and Physics*, 16, 11319–11336. <https://doi.org/10.5194/acp-16-11319-2016>
- 775 Nilsson, E. D., Rannik, Ü., Swietlicki, E., Leck, C., Aalto, P. P., Zhou, J., & Norman, M. (2001).
776 Turbulent aerosol fluxes over the Arctic Ocean: 2. Wind-driven sources from the sea. *Journal of
777 Geophysical Research: Atmospheres*, 106(D23), 32139–32154.
778 <https://doi.org/10.1029/2000JD900747>
- 779 Nyeki, S., Coulson, G., Colbeck, I., Eleftheriadis, K., Baltensperger, U., & Beine, H. J. (2005). Overview
780 of aerosol microphysics at Arctic sunrise: measurements during the NICE renoxification study.
781 *Tellus B*, 57(1), 40–50. <https://doi.org/10.1111/j.1600-0889.2005.00122.x>

- 782 O'Dowd, C. D., Facchini, M. C., Cavalli, F., Ceburnis, D., Mircea, M., Decesari, S., et al. (2004).
783 Biogenically driven organic contribution to marine aerosol. *Nature*, *431*(7009), 676–680.
784 <https://doi.org/10.1038/nature02959>
- 785 Ovadnevaite, J., Ceburnis, D., Martucci, G., Bialek, J., Monahan, C., Rinaldi, M., et al. (2011). Primary
786 marine organic aerosol: A dichotomy of low hygroscopicity and high CCN activity. *Geophysical*
787 *Research Letters*, *38*(21). <https://doi.org/https://doi.org/10.1029/2011GL048869>
- 788 Patterson, E. M., Marshall, B. T., & Rahn, K. A. (1967). Radiative properties of the arctic aerosol.
789 *Atmospheric Environment*, *16*(12), 2967–2977. [https://doi.org/10.1016/0004-6981\(82\)90048-8](https://doi.org/10.1016/0004-6981(82)90048-8)
- 790 Polissar, A. V., Hopke, P. K., & Harris, J. M. (2001). Source regions for atmospheric aerosol measured at
791 Barrow, Alaska. *Environmental Science and Technology*, *35*(21), 4214–4226.
792 <https://doi.org/10.1021/es0107529>
- 793 Prather, K. A., Bertram, T. H., Grassian, V. H., Deane, G. B., Stokes, M. D., DeMott, P. J., et al. (2013).
794 Bringing the ocean into the laboratory to probe the chemical complexity of sea spray aerosol.
795 *Proceedings of the National Academy of Sciences of the United States of America*, *110*(19), 7550–
796 7555. <https://doi.org/10.1073/pnas.1300262110>
- 797 Quinn, P. K., Miller, T. L., Bates, T. S., Ogren, J. A., Andrews, E., & Shaw, G. E. (2002). A 3-year
798 record of simultaneously measured aerosol chemical and optical properties at Barrow, Alaska.
799 *Journal of Geophysical Research D: Atmospheres*, *107*(11), AAC 8-1.
800 <https://doi.org/10.1029/2001jd001248>
- 801 Quinn, P. K., Shaw, G., Andrews, E., & Dutton, E. G. (2007). Arctic haze: current trends and knowledge
802 gaps. *Tellus B: Chemical and Physical Meteorology*. [https://doi.org/10.1111/j.1600-](https://doi.org/10.1111/j.1600-0889.2006.00236.x)
803 [0889.2006.00236.x](https://doi.org/10.1111/j.1600-0889.2006.00236.x)
- 804 Quinn, P. K., Bates, T. S., Schulz, K., & Shaw, G. E. (2009). Decadal trends in aerosol chemical
805 composition at Barrow, Alaska: 1976-2008. *Atmospheric Chemistry and Physics*, *9*, 8883–8888.
806 Retrieved from www.atmos-chem-phys.net/9/8883/2009/
- 807 Quinn, P. K., Bates, T. S., Coffman, D. J., Upchurch, L., Johnson, J. E., Moore, R., et al. (2019). Seasonal
808 Variations in Western North Atlantic Remote Marine Aerosol Properties. *Journal of Geophysical*
809 *Research: Atmospheres*, *124*(24), 14240–14261. <https://doi.org/10.1029/2019JD031740>
- 810 Rahn, K. A. (1981). Relative importances of North America and Eurasia as sources of arctic aerosol.
811 *Atmospheric Environment (1967)*, *15*(8), 1447–1455. [https://doi.org/10.1016/0004-6981\(81\)90351-6](https://doi.org/10.1016/0004-6981(81)90351-6)
- 812 Rolph, G., Stein, A., & Stunder, B. (2017). Real-time Environmental Applications and Display sYstem:
813 READY. *Environmental Modelling & Software*, *95*(1364–8152), 210–228. Retrieved from
814 <https://doi.org/10.1016/j.envsoft.2017.06.025>
- 815 Sjogren, S., Gysel, M., Weingartner, E., Baltensperger, U., Cubison, M. J., Coe, H., et al. (2007).
816 Hygroscopic growth and water uptake kinetics of two-phase aerosol particles consisting of
817 ammonium sulfate, adipic and humic acid mixtures. *Aerosol Science*, *38*, 157–171.
- 818 Stein, A. F., Draxler, R. R., Rolph, G. D., Stunder, B. J. B., Cohen, M. D., & Ngan, F. (2015). NOAA's
819 HYSPLIT Atmospheric Transport and Dispersion Modeling System. *Bulletin of the American*
820 *Meteorological Society*, *96*, 2059–2077. Retrieved from [https://doi.org/10.1175/BAMS-D-14-](https://doi.org/10.1175/BAMS-D-14-00110.1)
821 [00110.1](https://doi.org/10.1175/BAMS-D-14-00110.1)
- 822 Stokes, R. H., & Robinson, R. A. (1966). Interactions in aqueous nonelectrolyte solutions. I. Solute-
823 solvent equilibria. *Journal of Physical Chemistry*, *70*(7), 2126–2131.
824 <https://doi.org/10.1021/j100879a010>

- 825 Ström, J., Umegård, J., Tørseth, K., Tunved, P., Hansson, H. C., Holmén, K., et al. (2003). One year of
826 particle size distribution and aerosol chemical composition measurements at the Zeppelin Station,
827 Svalbard, March 2000-March 2001. *Physics and Chemistry of the Earth*, 28(28–32), 1181–1190.
828 <https://doi.org/10.1016/j.pce.2003.08.058>
- 829 Tanner, D. J., Jefferson, A., & Eisele, F. L. (1997). Selected ion chemical ionization mass spectrometric
830 measurement of OH. *Journal of Geophysical Research Atmospheres*, 102(5), 6415–6425.
831 <https://doi.org/10.1029/96jd03919>
- 832 Thompson, C. R., Shepson, P. B., Liao, J., Huey, L. G., Apel, E. C., Cantrell, C. A., et al. (2015).
833 Interactions of bromine, chlorine, and iodine photochemistry during ozone depletions in Barrow,
834 Alaska. *Atmospheric Chemistry and Physics*, 15, 9651–9679. [https://doi.org/10.5194/acp-15-9651-](https://doi.org/10.5194/acp-15-9651-2015)
835 2015
- 836 Tomasi, C., Lupi, A., Mazzola, M., Stone, R. S., Dutton, E. G., Herber, A., et al. (2012). An update on
837 polar aerosol optical properties using POLAR-AOD and other measurements performed during the
838 International Polar Year. *Atmospheric Environment*, 52, 29–47.
839 <https://doi.org/10.1016/j.atmosenv.2012.02.055>
- 840 Tremblay, S., Picard, J.-C., Bachelder, J. O., Lutsch, E., Strong, K., Fogal, P., et al. (2019).
841 Characterization of aerosol growth events over Ellesmere Island during the summers of 2015 and
842 2016. *Atmos. Chem. Phys.*, 19, 5589–5604. <https://doi.org/10.5194/acp-19-5589-2019>
- 843 Tunved, P., Ström, J., & Krejci, R. (2013). Arctic aerosol life cycle: linking aerosol size distributions
844 observed between 2000 and 2010 with air mass transport and precipitation at Zeppelin station, Ny-
845 Ålesund, Svalbard. *Atmospheric Chemistry and Physics*, 13(7), 3643–3660.
846 <https://doi.org/10.5194/acp-13-3643-2013>
- 847 Villani, P., Picard, D., Marchand, N., & Laj, P. (2007). Design and validation of a 6-volatility tandem
848 differential mobility analyzer (VTDMA). *Aerosol Science and Technology*, 41(10), 898–906.
849 <https://doi.org/10.1080/02786820701534593>
- 850 Virkkula, A., Van Dingenen, R., Raes, F., & Hjorth, J. (1999). Hygroscopic properties of aerosol formed
851 by oxidation of limonene, α -pinene, and β -pinene. *Journal of Geophysical Research Atmospheres*,
852 104(D3), 3569–3579. <https://doi.org/10.1029/1998JD100017>
- 853 Wehner, B., Philippin, S., & Wiedensohler, A. (2002). Design and calibration of a thermodenuder with an
854 improved heating unit to measure the size-dependent volatile fraction of aerosol particles. *Journal of*
855 *Aerosol Science*, 33(7), 1087–1093. [https://doi.org/10.1016/S0021-8502\(02\)00056-3](https://doi.org/10.1016/S0021-8502(02)00056-3)
- 856 Weingartner, E., Baltensperger, U., & Burtscher, H. (1995). Growth and Structural Change of
857 Combustion Aerosols at High Relative Humidity. *Environmental Science and Technology*, 29(12),
858 2982–2986. <https://doi.org/10.1021/es00012a014>
- 859 Wiedensohler, A., Covert, D. S., Swietlecki, E., Aalto, P., Heintzenberg, J., & Leck, C. (1996).
860 Occurrence of an ultrafine particle mode less than 20 nm in diameter in the marine boundary layer
861 during Arctic summer and autumn. *Tellus B*, 48(2), 213–222. [https://doi.org/10.1034/j.1600-](https://doi.org/10.1034/j.1600-0889.1996.t01-1-00006.x)
862 0889.1996.t01-1-00006.x
- 863 Willis, M. D., Burkart, J., Thomas, J. L., Köllner, F., Schneider, J., Bozem, H., et al. (2016). Growth of
864 nucleation mode particles in the summertime Arctic: a case study. *Atmospheric Chemistry and*
865 *Physics*, 16, 7663–7679. <https://doi.org/10.5194/acp-16-7663-2016>
- 866 Zheng, G., Wang, Y., Wood, R., Jensen, M. P., Kuang, C., McCoy, I. L., et al. (2021). New particle
867 formation in the remote marine boundary layer. *Nature Communications*, 12(1).

- 868 <https://doi.org/10.1038/s41467-020-20773-1>
- 869 Zieger, P., Väisänen, O., Corbin, J. C., Partridge, D. G., Bastelberger, S., Mousavi-Fard, M., et al. (2017).
870 Revising the hygroscopicity of inorganic sea salt particles. *Nature Communications*, 8.
871 <https://doi.org/10.1038/ncomms15883>
- 872 Ziemba, L. D., Dibb, J. E., Griffin, R. J., Huey, L. G., & Beckman, P. (2010). Observations of particle
873 growth at a remote, Arctic site. *Atmospheric Environment*, 44(13), 1649–1657.
874 <https://doi.org/10.1016/j.atmosenv.2010.01.032>
- 875